THE ROLE OF MAGNETIC PERTURBATIONS IN RUNAWAY ELECTRON AND SAWTOOTH DYNAMICS

Gergely Papp

Cover page: The ITER perturbation coils in an $n = 3$ configuration.
Black coils have clockwise-, red coils counter clockwise current. The
grey torus illustrates the equilibrium LCFS.

Some figures in this thesis are in colour only in the electronic version,
available online through the Chalmers Publication Library or
http://www.dissertations.se

THE ROLE OF MAGNETIC PERTURBATIONS IN RUNAWAY ELECTRON
AND SAWTOOTH DYNAMICS
Gergely Papp
Department of Applied Physics
Chalmers University of Technology

Abstract

As the world's fusion energy program is increasingly focused towards burning plasma experiments, it is important to address the remaining theoretical issues. In this thesis we focus on the effect of magnetic perturbations on the radial plasma transport.

The sudden loss of plasma confinement in large tokamaks can lead to the generation of a relativistic runaway electron beam that may cause serious structural damage. To suppress the runaway beam the application of resonant magnetic perturbations (RMP) has been suggested. In this thesis, the numerical analysis of the RMP is based on the relativistic, gyro-averaged drift equations for the runaway electrons in the 3D perturbed equilibria of the TEXTOR and ITER tokamaks. The results indicate that, in a properly chosen perturbation geometry, runaway electrons are rapidly lost from approximately the outer half of the confinement volume. Simulation studies of runaway evolution with self-consistent electric field in the presence of impurities have been carried out for the JET tokamak with a 1D tool, where we have demonstrated the runaway suppression effect of magnetic perturbation induced radial transport. We also show that runaway electrons can generate high energy positrons, and that their synchrotron radiation may be used for diagnostic purposes.

The last part of the thesis describes the low frequency precursor activity observed in the ASDEX Upgrade tokamak before sawtooth crashes, which are periodic density and temperature redistributions of the plasma core. Besides the well-known internal kink mode, the low frequency sawtooth precursor (LFSP) mode is studied in detail. Time-frequency analysis indicates non-linear interaction and a similar spatial structure for the two modes. A possible role of this mode in the evolution of the sawtooth crash is discussed in the context of magnetic perturbations.

Keywords: fusion plasma physics, tokamak, runaway electrons, runaway mitigation, magnetic perturbation, sawtooth oscillation

iv

Publications

This thesis is based on the work contained in the following papers:

[A] G. Papp, M. Drevlak, T. Fülöp, and P. Helander. Runaway electron drift orbits in magnetostatic perturbed fields. *Nuclear Fusion*, **51** 043004, 2011. http://stacks.iop.org/NF/51/043004.

[B] G. Papp, M. Drevlak, T. Fülöp, P. Helander, and G. I. Pokol. Runaway electron losses caused by resonant magnetic perturbations in ITER. *Plasma Physics and Controlled Fusion*, **53** 095004, 2011. http://stacks.iop.org/PPCF/53/095004.

[C] G. Papp, M. Drevlak, T. Fülöp and G. I. Pokol. The effect of resonant magnetic perturbations on runaway electron transport in ITER. *Plasma Physics and Controlled Fusion*, **54** 125008, 2012. http://stacks.iop.org/PPCF/54/125008.

[D] G. Papp, T. Fülöp, T. Fehér, P. C. de Vries, V. Riccardo, C. Reux, M. Lehnen, V. Kiptily, V. V. Pluysnin, B. Alper and JET EFDA contributors. The effect of ITER-like wall on runaway electron generation in JET. *Nuclear Fusion*, **submitted**, 2013.

[E] T. Fülöp and G. Papp. Runaway positrons in fusion plasmas. *Physical Review Letters*, **108** 225003, 2012. http://link.aps.org/doi/10.1103/PhysRevLett.108.225003.

[F] G. Papp, G. I. Pokol, G. Por, A. Magyarkuti, N. Lazányi, L. Horváth, V. Igochine, M. Maraschek, and ASDEX Upgrade Team. Low frequency sawtooth precursor activity in ASDEX Upgrade. *Plasma Physics and Controlled Fusion*, **53** 065007, 2011. http://stacks.iop.org/PPCF/53/065007.

Statement of contribution

I have carried out the simulations, data analysis- and presentation for papers A–D. I was also the main contributor in understanding the results of these simulations, prepared all the figures and wrote most of the text. In Paper E I have checked the analytical and numerical calculations made by the first author, and I have calculated the synchrotron spectra. In Paper F I have carried out a major part of the time-frequency analysis and proposed the model on the role of the LFSP in the sawtooth crash. I also prepared most of the figures and was responsible for writing the manuscript.

Related publications
(not included in the thesis)

1. G. Papp, M. Drevlak, T. Fülöp and G. I. Pokol. Runaway electron dynamics and transport anisotropy due to resonant magnetic perturbations in ITER. In *24th IAEA Fusion Energy Conference*, volume IAEA-CN-197, page TH/P4–05, San Diego (CA), USA, 2012.

2. T. Fülöp and G. Papp. Runaway positrons in tokamak plasmas. In *Europhysics Conference Abstracts*, volume 36F, page P4.067, Stockholm, Sweden, 2012. ISBN 2-914771-79-7

3. G. Papp, M. Drevlak, T. Fülöp, and G. I. Pokol. Spatial distribution of ITER runaway electron wall loads in the presence of 3D magnetic perturbations. In *Europhysics Conference Abstracts*, volume 36F, page P1.089, Stockholm, Sweden, 2012. ISBN 2-914771-79-7

4. G. Papp, M. Drevlak, T. Fülöp, P. Helander, and G. I. Pokol. Runaway electron losses enhanced by resonant magnetic perturbations. In *12th IAEA Technical Meeting on Energetic Particles in Magnetic Confinement Systems, IAEA-TM-40762*, page O.26, Austin (TX), USA, 2011.

5. G. Papp, G. I. Pokol, G. Por, A. Magyarkuti, N. Lazányi, L. Horváth, V. Igochine, M. Maraschek, and ASDEX Upgrade Team. Low frequency sawtooth precursor in ASDEX Upgrade. In *5th IAEA Technical Meeting on Theory of Plasma Instabilities*, page B4.1, Austin (TX), USA, 2011.

6. G. Papp, M. Drevlak, T. Fülöp, P. Helander and G. I. Pokol. The effect of resonant magnetic perturbations on runaway electrons. In *Europhysics Conference Abstracts*, volume 35G, p. P4.107, Strasbourg, France, 2011.

7. G. I. Pokol, G. Papp, G. Por, A. Magyarkuti, N. Lazányi, L. Horváth, V. Igochine, M. Maraschek and ASDEX Upgrade Team. Sawtooth precursors in ASDEX Upgrade. In In *Europhysics Conference Abstracts*, volume 35G, page P4.093, Strasbourg, France, 2011. ISBN 2-914771-68-1

8. G. Papp, M. Drevlak, T. Fülöp, P. Helander and G. I. Pokol. Runaway electron drift orbits in magnetostatic perturbed fields. In *23rd IAEA Fusion Energy Conference*, volume IAEA-CN-180, pages THW/P7–13, Daejeon, Korea, 2010.

9. G. Papp, G. Pokol, G. Por, V. Igochine and ASDEX Upgrade Team. Analysis of sawtooth precursor activity in ASDEX Upgrade using band-power correlation method. In *Europhysics Conference Abstracts*, volume 33E, page P1.157, Sofia, Bulgaria, 2009.

10. G. Pokol, G. Papp, G. Por, S. Zoletnik, A. Weller and W7-AS team. Experimental study and simulation of W7-AS transient MHD modes. *AIP Conference Proceedings*, 993(1):215–218, 2008.

Contents

x

Acknowledgements

I would like to thank my supervisors Tünde Fülöp, Gergő Pokol and Gábor Pór for all their help, guidance, encouragement and patience that they provided in all scientific and non-scientific matters as my "academic family". I have really enjoyed our common journey so far, and I do not believe a few sentences could express my gratitude.

I would like to thank my colleague and great friend Michael Drevlak for the everyday prompt assistance and Per Helander for all the wise and invaluable remarks. I would like to thank István Pusztai, Yevgen Kazakov, Albert Mollén, Sara Moradi, Imre Pázsit, Adam Stahl, László Horváth, Tamás Fehér, Håkan Smith and Matt Landreman for their friendship, their continuous help in everyday scientific questions and for all their comments on my papers and this thesis.

I was fortunate enough to spend stimulating research visits at several labs worldwide. I gratefully acknowledge the hospitality of all of them and particularly my hosts Valentin Igochine, Gabriella Pautasso & Philipp Lauber (IPP), Eric Hollmann (GA), Peter de Vries & Michael Lehnen (JET) and Peter Catto & Miklós Porkoláb (MIT). I would like to thank all my colleagues and students at Chalmers, BME-NTI and IPP for creating a stimulating and pleasant working atmosphere during the time we spent together. Special thanks to Tamás Tél for the eye-opening discussions on chaotic dynamics and László Bülgözdi as well as Csaba Sükösd who have inspired me to become a physicist.

Last but not least I would like to thank the love and support of my family who have been exemplary tolerant regarding my absence. This thesis is dedicated to my dearest love Orsi, who has always stood by my side, and who, I hope, always will.

Köszönetnyilvánítás

Szeretném megköszönni témavezetőimnek, Fülöp Tündének, Pokol Gergőnek és Pór Gábornak a rengeteg segítséget, biztatást és türelmet amit kaptam mind szakmai, mind személyes ügyekben. Rendkívül élveztem eddigi közös utunkat, de nem hiszem hogy hálámat néhány sorban ki tudnám fejezni.

Köszönöm Pusztai Istvánnak hogy elviselte a konstans magyarul motyogásomat a szobánkban, és köszönöm Pázsit Imrének a számtalan anekdotát amelyek nemcsak szórakoztatóak, de roppant tanulságosak is. Itt szeretném megköszönni magyarul értő diákjaimnak, különösen Horváth Lászlónak és Csépány Gergelynek a közös munkát – hiszem hogy én többet tanultam tőletek mint ti tőlem. Köszönettel tartozom Bülgözdi Lászlónak hogy megszerettette velem ezt a csodálatos tudományt, és Sükösd Csabának aki arra inspirált hogy fizikus legyek.

Szeretném megköszönni családomnak törődésüket és szeretetüket, hogy türelemmel viselik, amikor távol szakadok otthonról. Dolgozatomat drága Orsimnak ajánlom, akinek szeretetére és támogatására mindig számíthatok.

Abbreviations

Acronyms

ANTS   plasm**A** simulatio**N** with drif**T** and collision**S**
DED   **D**ynamic **E**rgodic **D**ivertor
ILW   **I**TER-**L**ike **W**all
KAM   **K**olmogorov-**A**rnold-**M**oser
LCFS   **L**ast **C**losed **F**lux **S**urface
LFSP   **L**ow **F**requency **S**awtooth **P**recursor
MHD   **M**agneto**h**ydro**d**ynamic(s)
RE   **R**unaway **E**lectron
RMP   **R**esonant **M**agnetic **P**erturbations
STFT   **S**hort **T**ime **F**ourier **T**ransform
SXR   **S**oft **X**-**R**ay

Tokamaks

ASDEX Upgrade   **A**xially **S**ymmetric **D**ivertor **EX**periment Upgrade,
                 Max Planck Institut Für Plasmaphysik (IPP),
                 Garching bei München, Germany
DIII-D   The **D**oublet **III** with **D**-shaped plasma
                 General Atomics, San Diego (CA), USA
ITER   "The Way" (latin)
                 Under construction in Cadarache, France
JET   **J**oint **E**uropean **T**orus,
                 Culham Science Centre, Abingdon, UK
TEXTOR   **T**okamak **EX**periment for **T**echnology **O**riented **R**esearch
                 Forschungszentrum Jülich, Germany

1 | Introduction

Given a task to do, one that seems impossible, given the desire to do it,
humans can accomplish almost anything.
– Jim Lovell, Apollo astronaut

The human civilization requires an ever increasing amount of energy. At present times most of our energy production is based on fossil sources, and this is not in accordance with the principle of sustainable development [1]. Fossil fuels will inevitably run out, but even before that, their use puts a large environmental load on our planet. One of the possible long-term options is the utilization of nuclear energy [2]. Exploiting nuclear fission is a technique in use since more than 50 years. **Nuclear fusion** of light nuclei is another option to employ nuclear energy. While keeping all the advantages of nuclear fission, such as energy production on a large scale or the small fuel requirement, it eliminates the problem of long-term nuclear waste and also has promising safety aspects [3, 4]. Up to our present knowledge, energy production based on controlled nuclear fusion possesses almost all the attributes of an ideal energy source [5–8]: it is safe, affordable, controlled, plentiful, pollution-free, requires a small amount of fuel and has a reasonable plant size.

The basic idea is about 90 years old [9] and is the easiest to understand through the Bethe-Weizsäcker semi-empirical binding energy formula [10]: uniting light nuclei into heavier ones releases a great amount of energy. The most practical option is to use isotopes of hydrogen, namely deuterium (^{2}H $\equiv$ D) and tritium (^{3}H $\equiv$ T):

$$D \; + \; T \;\; \rightarrow \;\; \alpha \; + \; n \; + \; 17.6 \text{ MeV},$$

where the reacton will produce an α-particle and a neutron (that carries 80% of the reaction energy). Unfortunately, the implementation of controlled nuclear fusion has proved to be rather challenging. The main problem is posed by the extremely high temperature (in the order of 100

1

million Kelvins) needed to overcome the strong Coulomb repulsion of the nuclei to be fused. Matter at this temperature is in the plasma state and cannot be held together by any kind of vessel made of solid materials. There are three main concepts to confine the fusion plasma. The first one is gravitational confinement that powers the stars, but is not feasible on planetary scales. The second is inertial confinement, where small fuel pellets are ignited by ultra intense lasers to form a "miniature hydrogen bomb". This method, though in principle is feasible on Earth, when realised with present day technologies raises questions of practicality and cost-effectiveness [6]. The third option, that is commonly believed to be the best solution today, is magnetic confinement.
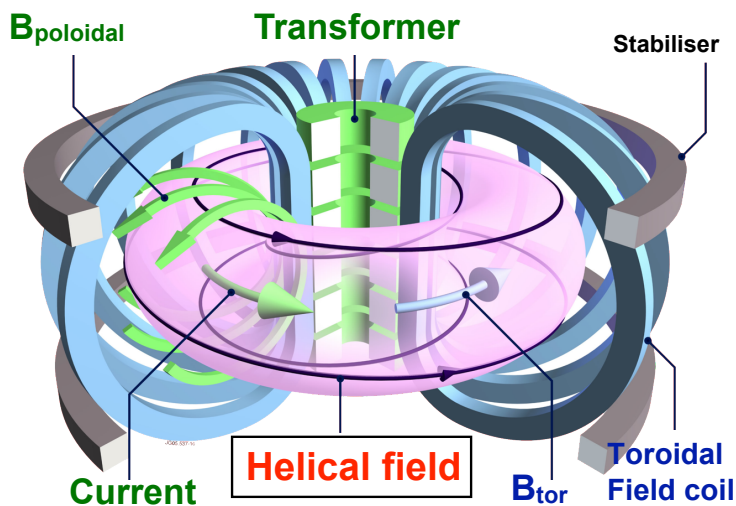

Figure 1.1: Schematic figure of a tokamak.

The most successful magnetic confinement device of present days is the tokamak [7], shown in figure 1.1. It uses a strong (up to 8 T), magnetic field bent to a torus shape. In a tokamak a large toroidal plasma current (up to 15 MA) is used to twist the magnetic field in a wreath-like helical structure to avoid particle losses due to motion along field lines and drifts. Along with the currently operating devices [11] the next step in fusion research is already under construction. The ITER tokamak is being built in Cadarache, France, in a worldwide collaboration that aims to explore reactor relevant operating conditions and to test reactor elements [12].

In order to operate an energy producing fusion reactor in a safe and efficient way, we need to precisely understand the behaviour of fusion plasmas. Although intensive research has been carried out in the last decades, there are still a number of open questions. This thesis attempts to describe the effect of magnetic perturbations on the tokamak magnetic structure and its effects on the transport of plasma particles by discussing two phenomena that contribute to the understanding of tokamak physics.

One of the applications is connected to **runaway electrons** [13], which is a high energy electron population in the plasma. Runaway electron generation is an interesting effect of collisional transport in fusion plasmas. The collisional drag force experienced by a sufficiently high energy electron decreases with increasing momentum due to the nature of Coulomb collisions in plasmas [14]. If a sufficiently high electric field parallel to the magnetic field is present in the plasma, there will be a population of electrons for which the electrostatic accelerating force is stronger than the collisional drag. These electrons will then continue to be accelerated up to relativistic energies. The runaway electrons usually drift to the wall of the tokamak, where the impact can cause serious damage [15]. Fortunately, the conditions necessary for substantial runaway production seldom arise during normal operation, but can appear during non-operational plasma conditions, such as disruptions [7]. Disruptions are global plasma instabilities capable of terminating the discharge. During the disruption a very quick cooling of the plasma takes place, so that the conductivity drops and, as a result, the toroidal electric field rises dramatically due to the self-inductance of the plasma. It can be shown that a higher plasma current leads to a higher number and more energetic runaways [16], therefore large tokamaks are more threatened by runaways than small ones. Unmitigated disruptions represent a severe risk for ITER [17], and should be avoided by reliable control of the plasma discharge. Before operating on reactor-relevant scales, a suitable solution has to be found to eliminate the runaway electrons [18].

Resonant Magnetic Perturbations (RMP) are one option for runaway electron mitigation. In RMP, a perturbation field generated by external coils is applied to the plasma, and as a result, the radial transport is enhanced. This has been shown to work well for runaway suppression in various experiments [19–24], while positive results in this respect are lacking in others, such as in the biggest currently operating tokamak, JET [25]. The reason for the difference in the experimental success of

suppressing runaways in various devices is an important question if we plan to apply RMP to aid runaway electron mitigation in ITER. Due to the complexity of particle transport in perturbed magnetic fields, a reliable model of how the runaway electrons are transported out of the plasma can only be obtained via three-dimensional numerical modelling of the runaway electron drift orbits. In the first, major part of this thesis, we study the effect of RMP on runaway electron transport and losses in order to create a reliable basis for RMP modelling and to estimate its effectiveness in ITER. We will also show the effect of magnetic perturbations on runaway electron generation in JET with two different wall materials (carbon and beryllium).

Interestingly, runaway electrons generated in tokamak disruptions give rise to the strongest – albeit not deliberate – man-made positron sources [26]. We calculate the distribution function of the positrons and show that their synchrotron radiation may be employed to gain information about plasma parameters that are hard to diagnose during a disruption.

The last topic covered in this thesis is the issue of **sawtooth oscillations** [27], or sometimes called as "internal disruptions". This phenomenon is responsible for periodically expelling particles and energy from the core of the plasma to outer regions, that has both advantages [28] and disadvantages [18, 29, 30] at the same time. For this reason, the aim is to control, rather than completely avoid sawteeth. The field of sawtooth control has made significant progress lately [31], but we are still lacking a thorough understanding of the underlying physics. Right after the very first observation [32] it became clear that the transient transport events – called *sawtooth crashes* – are connected to the appearance of an internal kink mode, which is a core magnetohydrodynamic (MHD) mode. This mode is taken into account in every sawtooth model. Recent results on the tokamaks ASDEX Upgrade [33–35], HT-7 [36] and JET [37] showed, that along the energetic internal kink mode, a low frequency signal component is also measurable, which gains energy just before the sawtooth crash. In the last part of the thesis, we describe the recent experimental results concerning this **Low Frequency Sawtooth Precursor (LFSP)** and introduce a possible model on how it can play a role in the sawtooth crash. We will show that this weak, perturbative fluctuation can be of large importance, thus understanding its behaviour can make an important contribution to present day's most favoured sawtooth crash models [33, 38].

Magnetic perturbations have an important role in both runaway electron and sawtooth dynamics. In a magnetic confinement fusion device the particle transport is extremely anisotropic. While particles can travel freely along the magnetic field lines with their thermal speed, in the direction perpendicular to the magnetic surfaces the transport is governed by collisions, leading to several orders of magnitude smaller transport coefficients in the perpendicular direction [14]. In other words, the plasma acts as an insulator in the radial direction, which is very favourable if we want to achieve 100 million degrees in the core, and at the same time, technically manageable temperatures just a few meters away at the edge. If the magnetic field structure is distorted either for internal or external reasons, that can lead to a formation of mixed magnetic topologies of magnetic islands and so-called **ergodic zones**. In these radially extended zones the magnetic field lines meander in a chaotic way, and particles following the ergodic field lines can be transported significantly faster in the radial direction. In other words, ergodic zones act like "transport short-circuits". The spatial properties – such as size and position – of the ergodic zones depend on the underlying perturbation strength and structure in a nonlinear way. As a result, even perturbations small compared with the equilibrium magnetic field can lead to the generation of ergodic zones. Deliberately generating ergodic zones at the plasma edge can ease the removal of runaway electrons before they are accelerated to very high energies, while ergodic zones generated by core MHD modes can play a role in the transient transport of the sawtooth crash.

The rest of the thesis is organized as follows. The effects of magnetic perturbations on the tokamak magnetic structure along with the generation and properties of ergodic zones are described in chapter 2. An introduction to the runaway phenomenon is given in chapter 3 with a short summary of the numerical results concerning the effect of RMP on runaway electrons. The sawtooth instability is described in chapter 4 along with the experimental results on the LFSP and its possible role in the crash models. Finally, a summary is given in chapter 5.

2 | Magnetic perturbations

Let us first introduce the classic definitions of the magnetic structure of the tokamak in the common plasma physics nomenclature. As was described in chapter 1, tokamaks realize magnetic plasma confinement in toroidal geometry. The definitions of the toroidal geometry are shown in figure 2.1a.
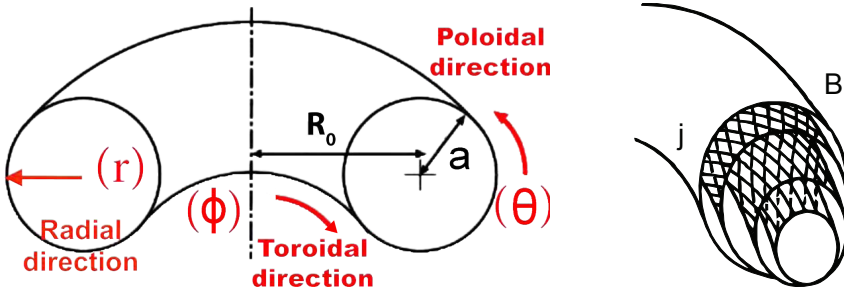

Figure 2.1: (a) Definitions of the toroidal geometry: radial (r), poloidal (θ) and toroidal (ϕ) directions; R_0 marks the major-, a the minor radius. (b) Nested magnetic surfaces drawn by magnetic field lines and current lines.

For axisymmetric equilibria – where physical quantities do not depend on the toroidal angle ϕ – the magnetic field lines necessarily lie in nested toroidal magnetic surfaces as illustrated in figure 2.1b [7]. Equivalently, if we follow a magnetic field line long enough, we will be able to observe it coming around a topologically torus surface, called the **magnetic surface**. The basic condition for equilibrium requires that the electromagnetic forces balance the plasma pressure: $\mathbf{j} \times \mathbf{B} = \nabla p$.

From this equation $\mathbf{B} \times \nabla p = 0$ follows, thus there is no pressure gradient along the field lines, the magnetic surfaces are surfaces of constant pressure. Also, $\mathbf{j} \times \nabla p = 0$, and consequently the current lines also lie on the magnetic surfaces as shown in figure 2.1b.

In tokamak equilibria, the successive surfaces are labeled by the values of any *surface quantity*, a quantity that changes monotonically as moving *across* the magnetic surfaces, but is constant on the magnetic surface. This is denoted by ψ, that plays the role of the radial coordinate. One possible choice for ψ, the one we will use in this thesis, is the **toroidal flux** Ψ_t, which is the magnetic flux through a surface perpendicular to the magnetic axis. For convenience, this quantity is made dimensionless $\psi = \Psi_\mathrm{t}/B_0 a^2$ where B_0 is the characteristic magnetic field and a is the minor radius of the device. In the case of a circular torus we have simply $\psi \equiv r^2$, where r is the dimensionless radial coordinate (scaled with a). In this coordinate system the magnetic axis is represented by $\psi = 0$ and the **last closed flux surface (LCFS)** by $\psi = 1$. The variables (ψ, θ, ϕ) form a curvilinear coordinate system, that can be made orthogonal by a proper choice of the angles.

An important parameter characterizing the field lines is the **safety factor**, q [8]. In an axisymmetric equilibrium, each magnetic field line has a value of q. The magnetic filed line spirals around its associated magnetic surface along a helical trajectory. The safety factor is defined as the average value of the change in its $\Delta\phi$ toroidal angle per a full poloidal transit $(\Delta\theta = 2\pi)$. With this definition, a magnetic surface consists of field lines with identical values of q. There are several different ways to express q in the most convenient form for a given application [7]. For a large aspect ratio $(R_0 \gg a)$ circular tokamak $q(r) \simeq rB_\phi/R_0 B_\theta$, where B_ϕ and B_θ are the toroidal- and poloidal magnetic field components, respectively. An alternative expression for q can be obtained in terms of the magnetic fluxes:

$$q = \frac{\mathrm{d}\Psi_\mathrm{t}}{\mathrm{d}\Psi_\mathrm{p}} \tag{2.1}$$

where Ψ_t and Ψ_p are the toroidal and poloidal fluxes. Thus the safety factor can be expressed as the rate of change of toroidal flux with poloidal flux. In other words q represent "*how many toroidal rotations are required for a full poloidal rotation*". If a magnetic field line returns to its starting position after exactly one rotation around the torus, then $q = 1$. If the safety factor is a rational number, namely $q = m/n, \ \ m, n \in \mathbb{Z}$, the field line joins up on itself after m toroidal and n poloidal rotations

around the torus. A surface is called a **rational surface** if the q associated with that surface is rational. Since the rational numbers $\mathbb{Q}$ form a dense subset of the real numbers $\mathbb{R}$, usually only the surfaces associated with *low order* rationals (small m, n) are denoted as "rational surfaces". Rational surfaces play an important role in plasma stability. They are also crucial in the understanding of how the magnetic field is distorted as a result of magnetic perturbations, as will be shown in this chapter.

To describe field line twist in stellarators the associated quantity of the *rotational transform*, $\iota\!\!\!/ = \iota/2\pi$ is commonly used, where ι (iota) is the poloidal angle change in one toroidal turn. It can be expressed by $\iota\!\!\!/ = 1/q$. At some places in what follows, using $\iota\!\!\!/$ instead of q will be more convenient.

2.1 The Hamiltonian nature of field lines

The stationary magnetic field $\mathbf{B}$ satisfies $\nabla \cdot \mathbf{B} = 0$ and $\mathbf{B} \cdot \nabla \psi = 0$, namely the divergence-free nature of the magnetic field and its tangency to the magnetic surface $\psi = \text{const}$. The magnetic field satisfying these constraints can be conveniently represented in the Clebsch form [39–42]

$$\mathbf{B} = \nabla \psi \times \nabla \theta - \nabla \Psi_{\mathrm{p},0}(\psi) \times \nabla \phi, \tag{2.2}$$

where the surface quantity

$$\Psi_{\mathrm{p},0}(\psi) = \int_0^\psi \frac{\mathrm{d}\psi'}{q(\psi')}$$

is the dimensionless poloidal flux (the magnetic field and the gradient operators are also made dimensionless by scaling them with B_0 and a, respectively). From equation (2.2) one finds the equations for the magnetic field lines expressed in the coordinates (ψ, θ, ϕ) by using elementary geometrical formulas. Using the toroidal angle as the running parameter, a field line is characterized by the two functions $\psi(\phi)$ and $\theta(\phi)$ obeying the following differential equations:

$$\frac{\mathrm{d}\psi}{\mathrm{d}\phi} = -\frac{\partial \Psi_{\mathrm{p},0}}{\partial \theta}, \quad \frac{\mathrm{d}\theta}{\mathrm{d}\phi} = \frac{\partial \Psi_{\mathrm{p},0}}{\partial \psi}. \tag{2.3}$$

These field line equations have a *Hamiltonian structure*: $\Psi_{\mathrm{p},0}$ plays the role of the Hamiltonian, ϕ the role of "time", and ψ and θ appear as a pair of canonical variables [42–44]. In the unperturbed case, when $\Psi_{\mathrm{p},0}$

is a surface quantity depending only on ψ, equations (2.3) represent a one degree of freedom – hence integrable – dynamical system:

$$\frac{\mathrm{d}\psi}{\mathrm{d}\phi} = 0, \quad \frac{\mathrm{d}\theta}{\mathrm{d}\phi} = W(\psi), \tag{2.4}$$

where the unperturbed **winding number** is defined as follows:

$$W(\psi) = \frac{\partial \Psi_{\mathrm{p},0}}{\partial \psi} \quad \Longrightarrow \quad \Psi_{\mathrm{p},0}(\psi) = \int_0^\psi W(\psi') \mathrm{d}\psi'. \tag{2.5}$$

Comparing (2.1) with (2.5) shows that the winding number is equivalent with the previously defined rotational transform $W \equiv \iota = 1/q$. ψ is analogous to an action variable, a constant of motion; the associated angle variable increases linearly in time. A Poincaré mapping ($\phi = 2\pi n$, $n \in \mathbb{N}$) of the unperturbed case can be acquired as

$$\psi_{n+1} = \psi_n, \quad \theta_{n+1} = \theta_n + W(\psi_{n+1}) \,(\mathrm{mod}\ 2\pi),$$

that represents the exact solution of the integrable Hamiltonian system [41]. Equation (2.4) expresses that in the unperturbed situation the radial position of the field line measured in ψ remains constant, while its poloidal angle θ changes with $W(\psi) \equiv \iota(\psi)$ after each toroidal turn. This was exactly the definition of the flux surface and the rotational transform, respectively.

The ideal structure is, however, strongly modified whenever some (even arbitrarily small) perturbation is present. The perturbation can be due to external features such as imperfections in the coils or deliberate external perturbations (as studied in Papers A–C) or to internal factors such as instabilities or fluctuations (as studied in Paper F). The perturbed magnetic field is also conveniently represented in the (2.2) Clebsch form, in which the Hamiltonian is replaced by a function of all three coordinates:

$$\Psi_{\mathrm{p},0} \;\rightarrow\; \Psi_{\mathrm{p}}(\psi, \theta, \phi) = \Psi_{\mathrm{p},0}(\psi) + \epsilon \delta \Psi_{\mathrm{p}}(\psi, \theta, \phi).$$

The perturbation Hamiltonian $\epsilon \delta \Psi_{\mathrm{p}}$ is a 2π periodic function of the variables θ and ϕ. The $\epsilon \in \mathbb{R}^+$ parameter is the dimensionless *stochasticity parameter*, which measures the strength of the perturbation. The corresponding equations of the field lines are now

$$\frac{\mathrm{d}\psi}{\mathrm{d}\phi} = -\epsilon \frac{\partial \delta \Psi_{\mathrm{p}}(\psi, \theta, \phi)}{\partial \theta} \tag{2.6}$$
$$\frac{\mathrm{d}\theta}{\mathrm{d}\phi} = W(\psi) + \epsilon \frac{\partial \delta \Psi_{\mathrm{p}}(\psi, \theta, \phi)}{\partial \psi}.$$

These are the equations of motion of a $1^1/_2$ degrees of freedom dynamical system (a Hamiltonian system of one degree of freedom depending periodically on ϕ), which is, generally, nonintegrable. It is possible to construct different mapping techniques to solve (2.6) that are valid depending on the nature of the perturbation [41, 45–47]. *However*, in the papers included in this thesis we use a direct integration of the magnetic field calculated from the plasma equilibrium and any perturbation currents. This way, though requiring more computational power, facilitates a faithful treatment of the magnetic field and allows us to study the effect of any arbitrary perturbation without restrictions.

The nature of the field lines is conveniently studied by considering a **Poincaré plot**, obtained by recording the values of the coordinates (ψ, θ) when the field line crosses a chosen poloidal cross-section ($\phi = $ const). These coordinates define the phase space of the dynamical system associated with the field lines. Poincaré mapping can be carried out for any arbitrary plasma shape. The Poincaré plot of the unperturbed system – after enough iterations – consists of a set of closed concentric curves (corresponding to non-rational magnetic surfaces) interspersed with discrete points (corresponding to rational surfaces). An alternative graphical representation, that in some cases provides a clearer picture, is obtained by making a cut starting from the center (the magnetic axis) pulling the two parts apart, and expanding the point representing the magnetic axis into a line. The radial coordinate ψ is represented on the vertical axis and the poloidal angle θ is given, modulo 2π, on the horizontal axis. Non-rational surfaces are now represented as horizontal segments, and the rational surfaces (periodic orbits) show up as points aligned horizontally. An example will be given in figure 2.2a.

2.2 Magnetic field perturbations

Due to the Hamiltonian nature of the (2.6) field line equations, the properties of the perturbed tokamak magnetic system are analogous to the phase space properties of perturbed Hamiltonian systems that are thoroughly studied in the literature and textbooks of nonlinear systems and chaos in conservative systems [48, 49]. One example is the well-known Chirikov-Taylor standard map [50, 51]:

$$\hat{\psi}_{n+1} = \hat{\psi}_n + \theta_n, \ \ \theta_{n+1} = \theta_n + \epsilon \sin(\hat{\psi}_{n+1}) \ \ (both \bmod 2\pi).$$

Although the standard map has some analogous properties, it is not a faithful model of a tokamak for several reasons. The most important is that $W(\psi)$ in a tokamak is – in standard scenarios – a monotonously decreasing function of ψ, which is not true for the standard map. Also, mapping techniques used in nonlinear dynamics most of the time apply a global perturbation. That is not the case in tokamaks, where the perturbation strength usually depends on ψ. In the case of core MHD modes the perturbation is dominant in the core, while in case of external perturbations it radially decays from the edge to the axis.

The rational or irrational nature of the magnetic surfaces is of great importance when it comes to the effects of perturbations. On rational surfaces the magnetic field lines sooner or later close exactly on themselves, thus the effects of any perturbation can accumulate, while on irrational surfaces the effects are averaged out more easily. As the result of the perturbation, the rational surfaces will break up, therefore they are often called **resonant surfaces**. Low order rationals break up more easily than high-order ones, and irrational surfaces require even stronger perturbation to break up [49].

The Kolmogorov-Arnold-Moser (KAM) theorem [52–54] determines exactly how the rational and irrational surfaces will break up depending on the perturbation strength. If the perturbation is sufficiently small ($\epsilon \ll 1$), then those magnetic surfaces will remain intact, for which

$$\left| W - \frac{r}{s} \right| > \frac{\mathcal{K}(\epsilon)}{s^{5/2}}, \tag{2.7}$$

where r/s is the rational approximation of the winding number or rotational transform $W \equiv \iota$ with an arbitrary precision. $\mathcal{K}(\epsilon)$ is a parameter that depends only on the perturbation strength and vanishes if $\epsilon \to 0$. This means that every r/s rational torus is surrounded by a $2\mathcal{K}(\epsilon)s^{-5/2}$ wide layer in which all the surfaces will break up. The unbroken surfaces are often called KAM surfaces or **KAM barriers**. The KAM theorem also implies that the total volume of the broken-up zones is nonzero for any arbitrarily small perturbation. What replaces the broken-up magnetic surfaces? The Poincaré-Birkhoff theorem [49] states that whenever $W(\psi)$ is a monotonic function, a $q = m/n$ rational surface breaks under a – sufficiently small – perturbation into an even number $2m$ of fixed points, m elliptical- or O-points alternating with m hyperbolic- or X-points. An example is shown in figure 2.2b. Hence the rational surfaces will be transformed into magnetic island chains. The O-point is surrounded by new KAM surfaces, while the X-point is surrounded
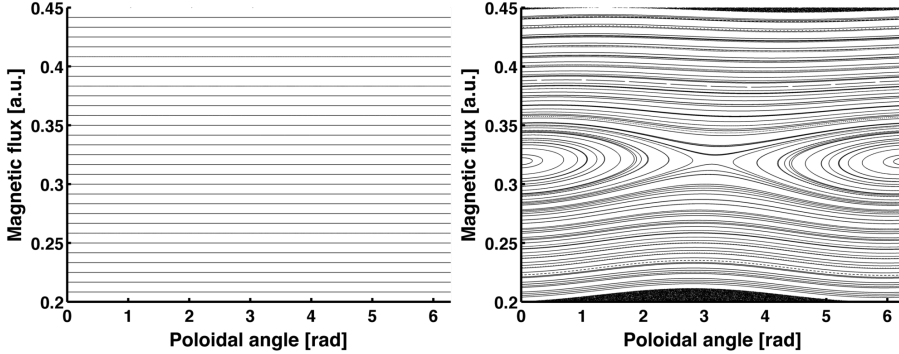
Figure 2.2: (Square) Poincaré plot of the (a) unperturbed and (b) perturbed magnetic field. An $m = 1$ magnetic island is visible with one X ($\theta \simeq \pi$) and one O point ($\theta \simeq 0$).

by an ergodic layer with nonzero phase volume. For sufficiently high perturbation the layer width might become macroscopic and it grows as the perturbation increases, up to the final destruction of the island chain. The stochastic layer always starts in the neighbourhood of the X points of the separatrix encircling the islands, they are the most "fragile" points of the chain. Whenever a perturbation is present, the topology of the magnetic field is strongly modified. There appear island chains (the locations of which are correlated with the rational values of q), together with undestroyed, but deformed magnetic surfaces at irrational q values and in between these features there exists ergodic zones filling up the space. This mixed magnetic topology of chaotic structures and unbroken surfaces is generic for tokamaks; understanding it is a prerequisite for any realistic study of transport in such devices.

The exact dependence of W on ψ, or, in tokamak language, the $q(\psi)$ **q-profile** is of great importance when it comes to the exact effect of the perturbations. A typical tokamak q-profile is shown in figure 2.3. Usually the q on axis, q_0 is around or under 1 ($W_0 \equiv \iota_0 \gtrsim 1$) and the q on edge, q_a is around 3–5 ($W_a < 1/3$). The q_0 value determines whether a $q = 1$ ($W(\psi) = 1$) surface is present in the plasma or not. According to the KAM theorem (2.7), it is the most sensitive to perturbation and is the first to break up. In chapter 4 we will see that the condition $q_0 < 1$ implies the possibility of sawtooth oscillations. The q-profile is flat in the core meaning that the low-order resonant surfaces lie far from each other. In the case of a perturbation that has sufficient amplitude in the plasma center (such as core MHD modes or weakly shielded
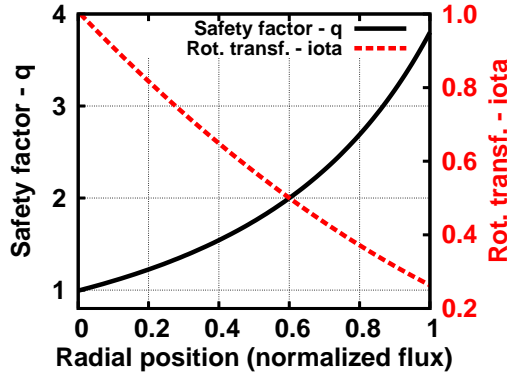
Figure 2.3: Typical tokamak q and rotational transform profiles.

external perturbations) relatively wide islands can be generated in the place of the broken up resonant surfaces, the locations of which are correlated with low-order rational values of the safety factor. These islands are separated by unbroken surfaces acting as KAM barriers. Prominent MHD modes such as resistive kink modes [55, 56] or Neoclassical Tearing Modes (NTM) [57] appear in this way. Core MHD modes will be discussed in chapter 4. We will show examples of island formation in figure 2.4.

Due to the shape of the q-profile the low-order rational surfaces are closer to each other at the plasma edge. With enough perturbation the last KAM barriers separating the clustered edge islands disappear, and the islands – which are completely replaced by ergodic zones themselves for sufficiently strong perturbation – meld together, forming a global ergodic zone at the plasma edge as highlighted in figure figure 2.4. Even if the width of islands and standalone ergodic layers could be estimated in a simple way, the overlapping and disappearance of KAM barriers cannot. The global evolution of the magnetic structure depends nonlinearly on the perturbation strength: as it increases we might observe sudden changes in the particle transport at certain thresholds due to the sudden disappearance of KAM barriers originally separating broad ergodic zones. The phenomenon of edge ergodic zones is the basis of techniques enhancing edge transport via external perturbations like the Dynamic Ergodic Divertor (DED) [58], the ELM pacing coils [59–63] or the Resonant Magnetic Perturbations (RMP) aiming at runaway mitigation. The latter is the topic of Papers A–C, and will be described in chapter 3.
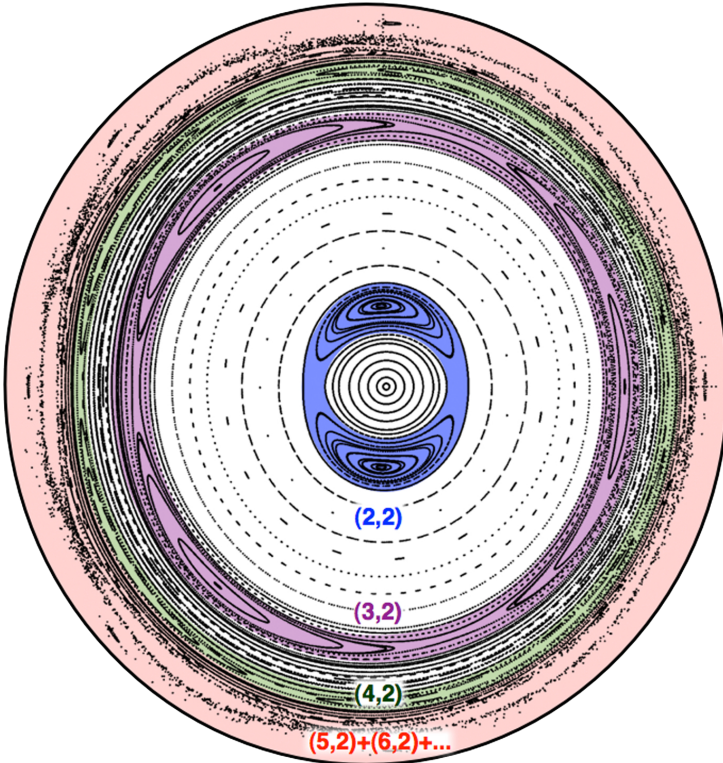
Figure 2.4: The result of a global perturbation with 180° toroidal symmetry $(n = 2)$ on a circular plasma, shown in a poloidal cross section. In the inner regions magnetic islands appear, with mode numbers $(m, n) = (2, 2)$, $(3, 2)$. At the edge, the overlapping magnetic islands create a broad ergodic zone outwards from $q = 2$. The outermost black line shows the unperturbed last closed flux surface as a comparison.

3 | Runaway electrons in disruptions

> *It is nice to know that the computer understands the problem.*
> *But I would like to understand it too.*
> – Eugene (Jenő) Wigner

The disruption is a global plasma instability that results in the loss of plasma confinement [7, 64, 65]. If the plasma reaches a stability limit it may begin to interact with the vessel wall, thereby causing an influx of wall particles. As a result of the heat conduction and the radiation due to influx of impurity particles, the plasma quickly loses a significant fraction of the stored thermal energy. During this *thermal quench* phase of the disruption, the temperature falls on a short, $\mathcal{O}(\mathrm{ms})$ time scale. Since the resistivity η depends on the temperature T ($\eta \sim T^{-3/2}$), it increases drastically in the cooling plasma. On these short time scales the inductive property of the plasma prevents the current from changing. Hence, when the resistivity rises, Ohm's law $E_\parallel = \eta_\parallel j_\parallel$ implies that an increasing parallel electric field will be induced. As will be described in the following section, runaway electrons (RE) are produced if the electric field is above a certain limit $E_\parallel > E_{\mathrm{c}}$. Disruptions can be harmful for a tokamak in several ways [18]. The heat loads on the vessel and the divertor due to radiation and heat conduction can be tremendous [66], halo currents may lead to excessive mechanical forces [67, 68], and if the induced toroidal electric field produces runaway electrons, these may severely damage the first wall upon impact [15, 69, 70].

3.1 The runaway electron phenomenon

The mathematical treatment of runaway electron generation is possible through the kinetic theory of plasmas, where the particles of species 'a' are described by the distribution function $f_a(\mathbf{r}, \mathbf{v}, t)$. If the number of charged particles of the species 'a' is conserved in a plasma, and the acceleration is due to electromagnetic forces, the distribution function obeys the Vlasov equation

$$\frac{\mathrm{d}f_a}{\mathrm{d}t} = \frac{\partial f_a}{\partial t} + \mathbf{v} \cdot \nabla f_a + \frac{q_a}{m_a}(\tilde{\mathbf{E}} + \mathbf{v} \times \tilde{\mathbf{B}}) \cdot \frac{\partial f_a}{\partial \mathbf{v}} = 0, \qquad (3.1)$$

where q_a and m_a are the charge and the mass of the particle respectively, and $\tilde{\mathbf{E}}$ and $\tilde{\mathbf{B}}$ are the electric and magnetic fields. These electric and magnetic fields include the small-scale (less than the Debye length) fluctuations responsible for interaction of individual particles. If we separate the effects of the short-scale fluctuations, or collisions, and include them in a separate collision operator $\mathcal{C}_a(f_a) = (\partial f_a/\partial t)|_{\mathrm{coll}}$, we arrive at the **Boltzmann equation**

$$\frac{\partial f_a}{\partial t} + \mathbf{v} \cdot \nabla f_a + \frac{q_a}{m_a}(\mathbf{E} + \mathbf{v} \times \mathbf{B}) \cdot \frac{\partial f_a}{\partial \mathbf{v}} = \mathcal{C}_a(f_a), \qquad (3.2)$$

which now includes only the $\mathbf{E}$ and $\mathbf{B}$ macroscopic average electric and magnetic fields. All quantities included in the Boltzmann equation can be measured, and it is the basic equation of kinetic theory.

For Coulomb collisions in plasmas the $\mathcal{C}_a$ collision operator can be modelled by the Fokker-Planck operator [14]. The kinetic equation (3.2) is then often called the **Fokker-Planck equation**. In some cases – usually in the description of processes involving shorter time scales than the characteristic collision times – the $\mathcal{C}_a(f_a)$ collision term can be omitted, and the (3.2) Boltzmann equation takes the form of the (3.1) Vlasov equation. Finding a suitable approximation of the Fokker-Planck operator is a complex topic [14]. Only one aspect of it is introduced in this section, which is essential for the understanding of the generation of runaway electrons.

Runaway electron generation

The friction force on an electron with velocity v is associated with the slowing down frequency (inverse of the characteristic slowing down time).

It comes mainly from collisions with other electrons [14]:

$$\frac{m_{\mathrm{e}} \left\langle \Delta v_{\parallel} \right\rangle^{\mathrm{ee}}}{\Delta t} = -m_{\mathrm{e}} v \nu_{\mathrm{s}}^{\mathrm{ee}} \propto G(x_{\mathrm{e}}), \qquad (3.3)$$

where $\nu_{\mathrm{s}}^{\mathrm{ee}}$ is the slowing down frequency from electron-electron collisions, $x_{\mathrm{e}} = v_{\mathrm{e}}/v_{\mathrm{Te}}$ and $G(x_{\mathrm{e}})$ is the Chandrasekar function:

$$G(x) \equiv \frac{\mathrm{erf}(x) - x \cdot \mathrm{erf}'(x)}{2x^2} \rightarrow \begin{cases} \frac{2x}{3\sqrt{\pi}}, & x \rightarrow 0 \\ \frac{1}{2x^2}, & x \rightarrow \infty \end{cases} \qquad (3.4)$$

$$\mathrm{erf}(x) \equiv \frac{2}{\sqrt{\pi}} \int_0^x e^{-y^2} \mathrm{d}y.$$

As can be seen from the asymptotic forms, the (3.4) Chandrasekar function is non-monotonic. The fact that $G(x)$ decreases for large arguments has the remarkable consequence that the (3.3) average friction force exerted on electrons decreases with increasing momentum, if the latter is sufficiently high. Figure 3.1 shows the friction force experienced by an electron as a function of its kinetic energy.
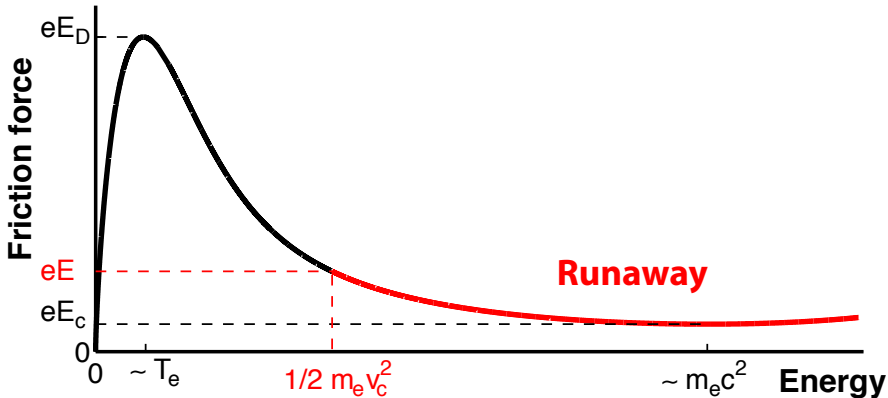

Figure 3.1: A sketch of the friction force as a function of electron energy.

The friction force vanishes in the limit of infinite velocity, unless relativistic effects are considered. The physical reason for this is that a fast electron spends less time in the vicinity of each particle it collides with than a slow electron does. If relativistic effects are taken into account, the friction force does not go down to zero: it reaches a minimum at energies around the rest energy [14, 71].

Now consider what happens if a constant electric field E is applied to the plasma. Sufficiently fast electrons above a certain critical velocity v_{c} experience a friction force smaller than the force from the electric field. Since the collision frequency decreases rapidly with increasing velocity, the faster the electron moves, the more time it has to gain momentum from the electric field before its next collision. The momentum gained between two collisions increasingly exceeds the momentum lost in each collision. This is an unstable situation: electrons are accelerated to high energies (tens of MeV) and form a population of so-called **runaway electrons**. Ultimately, runaway electrons reach relativistic speeds and are lost to the first wall, or are sometimes scattered by various plasma instabilities.

The maximum of the friction force is located at about the thermal energy level T_{e}. If the electric field is sufficiently strong, so that the critical speed is equal to the thermal speed, ordinary thermal electrons will also run away. This occurs when the electric field exceeds the so-called Dreicer field [13, 72]

$$E_{\mathrm{D}} = \frac{n_{\mathrm{e}} e^3 \ln \Lambda}{4 \pi \epsilon_0^2} \frac{1}{T_{\mathrm{e}}}, \tag{3.5}$$

where n_e is the electron density, e the electron charge, $\ln \Lambda$ is the Coulomb logarithm (typically $10 < \ln \Lambda < 25$) and T_{e} is the electron temperature. If relativistic effects are taken into account and the friction force does not fall all the way to zero at large energies, there is a minimum as the velocity approaches the speed of light. Thus, in order to produce runaway electrons the electric field must exceed the friction force on electrons travelling close to the speed of light [73]. The smallest electric field needed for runaway generation is determined by the minimum of the friction force and is found when the critical energy is equal to the rest energy. It is called the critical field E_{c}:

$$E_{\mathrm{c}} = \frac{n_{\mathrm{e}} e^3 \ln \Lambda}{4 \pi \epsilon_0^2} \frac{1}{m_{\mathrm{e}} c^2}. \tag{3.6}$$

The electric field needed to drive the current in an Ohmic tokamak plasma is usually not (much) above E_{c}, implying only a trace amount of runaways. However, when a disruption occurs, the induced parallel electric field $E_{\parallel}$ is often higher than E_{c}, suggesting that runaway electrons can be generated in significant amounts.

Primary generation of runaway electrons may occur through different mechanisms. The classical primary generation (often called *Dreicer*

generation) works in quasi-steady state, when an electric field larger than the critical field exists $E_\parallel > E_c$. In this mechanism the tail of the Maxwellian distribution of the plasma electrons can run away above a critical velocity determined by the electric field according to figure 3.1. The tail of the thermal electron distribution function lost to the runaway electrons is continuously recovered through collisional processes. Electrons diffuse in velocity-space above v_c and are accelerated by the electric field. This leads to a continuous influx to the runaway region. If the plasma cools rapidly, such as in disruptions, the quasi-steady state assumption is no longer valid, and a burst of runaways can be produced through the hot-tail generation [74–77]. Other possible primary generation mechanisms can be included as an $S_a(f_a)$ source term in equation (3.2), such as inverse Compton scattering by energetic γ rays, tritium decay, etc.

Although primary generation is clearly necessary to start the process, in large tokamak disruptions secondary generation by the avalanche mechanism quickly joins in, and finally produces a large fraction of runaway electrons. The secondary runaway generation is caused by close Coulomb collisions between existing runaways and thermal electrons. A runaway electron usually has such a large energy that it can, in one close collision, knock a thermal electron over the runaway threshold, while still remaining above the threshold itself. This leads to a runaway avalanche [16]. Small changes in the primary runaway sources can be magnified through the secondary generation. Reducing the avalanche effect bears a great importance from the runaway electron mitigation point of view.

3.2 Runaway positrons

The energetic electrons produced in the avalanches may give rise to electron-positron pair production. Pair production can occur in collisions between runaway electrons and thermal ions if the runaway energy exceeds three times the electron rest mass, $\mathcal{E}_e \gtrsim 1.5$ MeV. In tokamak disruptions the typical runaway energy is well above the threshold for pair-production and therefore positrons, in principle, should be present in large quantities [26] if the runaway electron current is large and the number of high-Z impurities is significant.

The aim of Paper E was to determine the distribution of positrons at birth, their subsequent fate and the possibility of detection through synchrotron radiation. The production rate is calculated by using a pair-

production cross-section valid for arbitrary energies [78] and a runaway electron distribution typical for avalanching [79], which is illustrated in figure 3.2. We have found that the ultrarelativistic cross-section used in
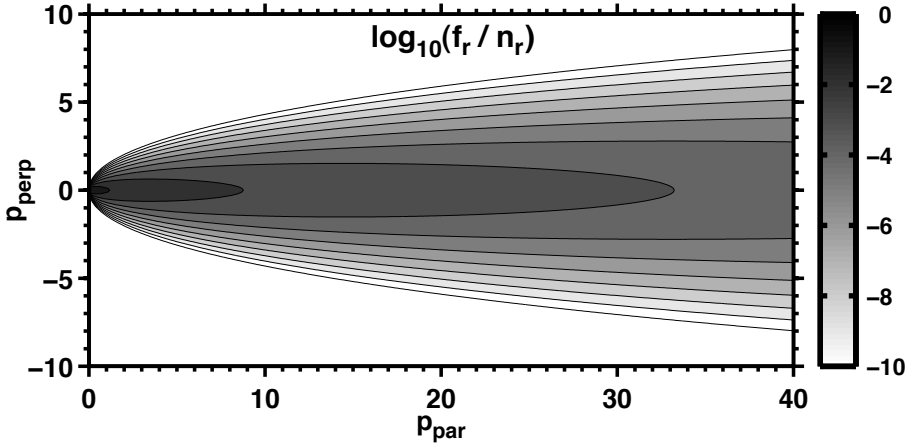

Figure 3.2: Contour plot of the avalanche distribution function from ref. [79] plotted with respect to parallel and perpendicular momenta normalized to $m_e c$ for $Z_{\mathrm{eff}} = 2$, $E/E_c = 60$, $T_e = 10$ eV.

ref. [26] overestimates the positron production. However, collisions with thermal electrons and impurities give a large contribution to the number of positrons created. The pair-production cross-sections scales with Z^2, where Z is the charge number of the nucleus, independent of the ionisation state. Due to the substantial amount of high-Z impurities present in the post-disruptive plasmas, the multiplicative factor associated with the plasma ions can be two orders of magnitude.

The positrons generated by runaway electron avalanches are relativistic already at birth, and in addition they experience acceleration by the electric field. To obtain the positron velocity distribution, the Fokker-Planck equation (3.2) including the positron production and annihilation rates and slowing-down terms is solved. The steady-state numerical solution to the kinetic equation have shown that most positrons that survive the slowing down without annihilation have energies less than 5 MeV. The lifetime of a positron can be estimated from the annihilation cross-section and it is expected to be of the order of seconds. If the electric field is strong enough, almost all the positrons run away in the opposite direction to the electrons.

Detection of the annihilation radiation of runaway positrons in tokamaks is difficult, because it is overwhelmed by the Bremsstrahlung radiation from the electron population. On the other hand, the synchrotron radiation of runaway positrons is peaked in the direction opposite from that of the runaway electrons and this may be possible to detect. We have estimated the synchrotron spectrum of the positron distribution with an approximative formula valid in toroidal geometry [80, 81]. Paper E presents the first runaway distribution integrated synchrotron spectrum calculation. In most cases, the maximum of the synchrotron radiation spectrum is around 1 μm, while the peak value of the synchrotron radiation spectrum is larger in plasmas with a large number of impurities, high magnetic field and high temperature.

The positrons may prove to be beneficial in tokamaks where the cameras capable of detecting runaway synchrotron generation are aligned opposite to the runaway electrons. For example, the currently operating largest tokamak, JET, has such infrared cameras and these would be suitable for detecting synchrotron radiation from runaway positrons. JET can also have runaway electron currents in the megaampere range and has sometimes large high-Z material content during massive gas injection or due to tungsten sputtering from the divertor. If the positron synchrotron radiation could be detected, it would give valuable information about the post-disruption plasma and the runaway electron population.

3.3   Simulation of runaway electron drift orbits

As was mentioned in chapter 1, externally applied Resonant Magnetic Perturbations (RMP) are one option for runaway electron mitigation. A large number of promising experiments [19–24] suggest that the application of RMP is capable of decreasing or even stopping the avalanching of runaways. However, the results are not uniformly positive in every tokamak [25]. The reason for the difference in the experimental success of suppressing runaways in various devices is not yet properly understood.

In the case of externally applied perturbations, as introduced in chapter 2, edge ergodic zones can form and significantly enhance the radial particle transport. Previous theoretical work has indicated that if the radial diffusion of runaway electrons is sufficiently strong, avalanches can be prevented and the magnetic perturbation level necessary for this has been estimated to $\delta B/B = 10^{-3}$ for typical tokamak parameters [82, 83].

However, the analytically estimated diffusion coefficient is an approximation and depends on many parameters. In the simplest picture, the electrons follow stochastic magnetic field lines and diffuse radially out of the plasma with the Rechester-Rosenbluth diffusion coefficient [84]. Due to the complexity of the effect of magnetic drift on diffusion, a reliable picture of how the runaway electrons are transported out of the plasma can only be obtained via three-dimensional numerical modelling of the runaway electrons.

Solving the complete kinetic problem of runaway electrons is a complex and computationally very expensive numerical task [85–89]. In the work presented in Papers A–C we solve the relativistic, gyro-averaged equations of motion for the runaway electrons including the effect of radiation losses and collisions. In these simulations we follow a test particle approach: independent test particles with given initial conditions for position $\mathbf{r}_0$ and velocity $\mathbf{v_0}$ are launched and their orbits are integrated in predefined 3D static magnetic fields. The particles are considered lost if they leave the computational zone, that is the field mesh truncated by the original last closed flux surface (LCFS) of the device. In Paper A the electric field $E_\parallel$ is set to be constant in time. In Papers B & C we use a time-dependent electric field obtained for an ITER-like disruption scenario calculated with a model of the coupled dynamics of the evolution of the radial profile of the current density (including the runaways) and the resistive diffusion of the electric field [90]. The model and the JET simulation results acquired with it are reported in Paper D and will be described in section 3.6.

At the high (tens of MeV) energies reachable by runaways the effect of synchrotron radiation [91] has to be taken into account. The average rate of change of momentum due to **synchrotron radiation** can be calculated from the Abraham-Lorentz force [92] as described in Appendix A of Paper A. In large tokamaks, such as ITER – studied in Papers B & C – also the effect of Bremsstrahlung [71, 93] radiation has to be considered. Bremsstrahlung is included in the form of a decelerating force, as is described in Paper B. The radiation terms have a measurable, but not significant effect on the results, especially if an electric field is present. We have found that including radiation terms has a negligible influence on the effect of RMP on the particle trajectories even in the ITER case.

The ANTS code

For the numerical solution of the relativistic drift equations the ANTS (plasmA simulatioN with drifT and collisionS) code [94] was selected. ANTS calculates the drift motion of particles in 3D fields and takes into account collisions with background (Maxwellian) particle distributions, using a full-f Monte Carlo approach. For the purposes of our work it has been extended to include the aforementioned radiation losses and a new collision operator that is valid for both thermal and relativistic velocities, as described in Appendix B of Paper A. Several minor modifications were necessary to address possible numerical issues when simulating tens of MeV runaway electrons.

One reason for our choice was that the ANTS code is highly modular. This flexibility allows one to run it with different sets of differential equations and Monte Carlo operators describing the drift motion and collisions of the test particles with the background, which was beneficial in e.g. comparison calculations. ANTS is also able to use the entire range of coil types available from the ONSET and EXTENDER coil optimisation packages [95, 96] in order to describe the external magnetic field. This was very advantageous in the implementation of different RMP systems. Furthermore, the 3D magnetic field is defined on a mesh in the entire domain of computation, and the integration of the particle orbits is carried out in Cartesian coordinates. This approach provides the greatest flexibility and facilitates a faithful treatment of magnetic fields with islands and ergodic zones, since the existence of magnetic surfaces is not required. If stellarator symmetry ($B(\theta, \varphi) = B(-\theta, -\varphi)$ [97]) can be assumed, like in Paper A, the memory demand of the calculations is reduced to some hundred MBs. The pseudo random number generator is initialised from the particle index, and therefore every individual particle trajectory in every run can be reproduced regardless of the stochastic nature of the collisions. This feature allows the investigation of single particle orbits in greater detail, if necessary.

3.4 Runaway losses in TEXTOR

In Paper A, we studied the runaway electron drift orbits in TEXTOR-like perturbed magnetostatic fields and evaluated the effect of RMP coils on runaway loss enhancement. The main reason for this choice is that it has been shown experimentally on TEXTOR that runaway losses can be enhanced by the application of RMP [21–24, 98]. The

measurements have shown that the runaway plateau current drops with increased perturbation current, and at sufficiently high perturbation levels the high energy runaways are suppressed. Interestingly, the current decay rate was unaffected by the perturbation [24]. Both the runaway plateau length and the measured synchrotron radiation intensity showed a significant drop at the same threshold perturbation.

A possible explanation of the observed phenonema is that the radial spread of the runaways is increased by increasing perturbation, decreasing the avalanche generation that depends on the runaway current and at a certain point avalanche generation is overwhelmed by the losses. Meanwhile, the threshold may be connected to a characteristic perturbation strength where a region of unbroken surfaces disappears and the neighboring ergodic zones meld together to form a large ergodic zone, which thus leads to a sudden increase in radial transport. The collection of published experimental results at TEXTOR concerning RMP and runaways makes it (in principle) possible to benchmark the numerical results. In the previous works [21, 22] analyzing the dynamics of runaways under the effect of RMP the authors used a mapping method based on Hamiltonian guiding center equations [99–101]. Instead of particle mapping we used the gyro-averaged equations of motion in the 3D perturbed field as well as included the effect of collisions and radiation.

The plasma parameters were chosen to be similar to the ones where the runaways were shown to be suppressed [24] by resonant magnetic perturbations created by the Dynamic Ergodic Divertor (DED) [58] coils. The unperturbed magnetic equilibrium has been calculated by the VMEC [102] equilibrium code. VMEC can only generate equilibria with unbroken flux surfaces and therefore it cannot properly take the effect of perturbation coils into account. We have created free boundary equilibria without the toroidal field ripple. This allows us to study the "pure" effect of the RMP. The effect of ripple on fast particles have been studied extensively in previous work [103–106]. We note that the ripple resonance effect is not significant at the particle energies we studied in our cases [106]. The magnetic field perturbations are modelled to be similar to the ones produced by DED-coils on TEXTOR in the 6/2 DC operation mode [58, 107], that has a 180° toroidal rotation symmetry, hence the generated islands have a lead toroidal mode number of $n = 2$. The coils create magnetic perturbations at the plasma periphery on the high field side of the torus that decay radially toward the inside of the plasma. We neglect the effect of shielding of magnetic field perturbations

by plasma response currents. This approximation is expected to be valid in cold post-disruption plasmas [24]. Including shielding of any strength would reduce the perturbation [108–110], thus our results should be interpreted as an upper limit on the actual losses. Close to the maximal DED current the coils are capable of creating the $\delta B/B = 10^{-3}$ magnetic perturbation level that is predicted to be necessary for runaway suppression [82] up to the flux surface $\psi = 0.7$, that roughly corresponds to the outer half of the confinement *volume*. A perturbed TEXTOR-like equilibrium was illustrated previously in figure 2.4 for 6 kA DED current. Clearly, the edge region becomes ergodic and particles outside the last intact magnetic surface can leave the plasma rapidly.

The drift topology for high energy particles can significantly differ from the magnetic topology in both perturbed and unperturbed magnetic fields [111, 112]. Therefore, we present **particle Poincaré plots** that allow us to determine how the confinement changes with different particle energies and perturbation currents. The particle Poincaré plots are not generated by a mapping algorithm, rather by recording the (ψ, θ) coordinates when the particles cross a fixed $\phi = \phi_P$ toroidal cross-section.
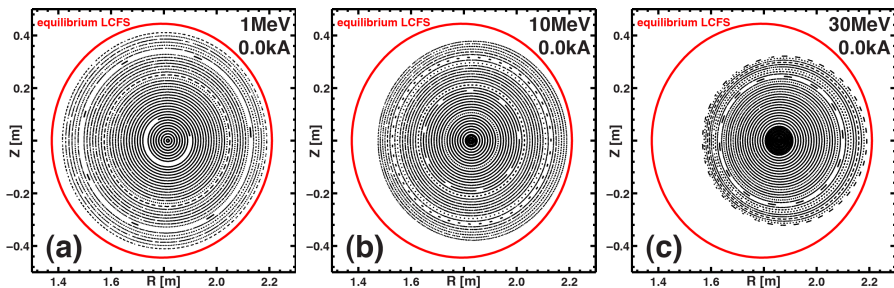

Figure 3.3: Poincaré plots of the particle orbits without RMP. The particle energies are (a) 1, (b) 10 and (c) 30 MeV. The confinement volume shrinkage is clearly observable.

Even in the unperturbed case, the confinement volume shrinks as the particle population is shifted with increasing energy, as illustrated in figure 3.3. Runaway electrons move antiparallel to the current and their drift orbits are therefore always shifted to the low field side as a result of adiabatic toroidal angular momentum conservation. If the displacement is defined as the distance between the center of the runaway orbit and the magnetic axis, then it is estimated to be $d \simeq q p_{\parallel}/eB_0$ [112, 113], where $p_{\parallel}$ is the non-normalized parallel momentum. The drift orbits

(in the unperturbed field) of the particles are circles that are displaced horizontally with respect to the flux surfaces, with a displacement that is proportional to the energy, for $\gamma \gg 1$ relativistic particles. Since the population is shifted, the outermost particles intersect the original LCFS that causes a shrinkage of the effective confinement zone. This shrinkage of the confinement zone plays an important role at high particle energies regardless of the DED. However, high energy particles are kept confined within their new LCFS, **hence the core runaways are not lost due to the RMP**. The effect of the DED decreases with increasing particle energy, at higher energies the edge stochastization is less visible. We found that the DED can significantly influence only the low-energy ($\simeq 1$ MeV) particles closer to the boundary. For these particles the onset time of the losses is dependent on the amplitude of the magnetic perturbation. For particles launched close to the edge the start of the losses decreased only by $\sim 20\%$. The time dependence of the following losses – the runaway current damping rate – is insensitive to the magnetic perturbation level. This and its experimentally measured value is consistent with our simulations. The simulations described in Paper A did not show the loss of core runaways. On the other hand, enhanced radial transport, even if it does not lead to drift orbit losses, may weaken localised runaway currents and it therefore weakens avalanche generation. Also, the loss of the core runaways is enhanced by MHD perturbations onset by the disruption [114]. These perturbations can expel a significant amount of runaways from the core to the edge in a small scale device like TEXTOR. Several tokamaks have reported enhanced runaway losses connected to various plasma waves [115–119]. The RMP can enhance the losses of the runaways once those are close to the edge. This may also explain the observed enhancement of runaway losses due to the RMP on small tokamaks. For JET, the MHD perturbations are not sufficient to expel the particles from the core, which could be one of the reasons why RMP does not seem to be effective in JET.

3.5 Loss estimations for ITER

Large tokamaks, such as ITER, could be more susceptible to substantial runaway electron generation than present tokamaks. The uncontrolled loss of a high energy electron population with a current of several megaamperes is intolerable and therefore the issue of how to avoid or mitigate the runaway generation is of prime importance for ITER.

The ITER ELM perturbation coils, in principle, can be used to aid runaway mitigation efforts. Extrapolating from experiments in existing devices and theoretical studies made for those carries large uncertainties due to the complexity of runaway dynamics and the chaotic nature of magnetic perturbations. Obviously, no experimental results are available about the runaway suppression capabilities of any ITER system. Therefore in Paper B and Paper C we carried out an investigation covering several possible current schemes, to estimate the RMP efficiency on runaway removal in ITER. For the purposes of Paper B, ANTS have been further extended to include the effect of Bremsstrahlung radiation that can be important for the ITER case. However, the results indicated that the particle loss dynamics is not much altered by the radiation effects. Also, we use a time-dependent electric field obtained for an ITER-like disruption scenario calculated with a model of the coupled dynamics of the evolution of the radial profile of the current density (including the runaways) and the resistive diffusion of the electric field [90].

The simulations have been carried out for the ITER scenario #2 (15 MA inductive burn) [120]. Inductive scenarios are expected to produce the largest and most energetic populations of runaway electrons. We use a cold (10 eV [18]) post-disruption equilibrium calculated with VMEC, based on plasma parameters obtained by simulations with the ASTRA code [120, 121]. The ELM perturbation coil-set consists of 9×3 quasi-rectangular coils at the low field side, that allows for a wide variety of possible current configurations. Due to the 9×3 alignment, the natural static configurations have $n = 9$ or $n = 3$ lead toroidal mode-number. In Paper B we investigated two $n = 9$ and four possible $n = 3$ configurations. The technically achievable upper limit of 60 kA for the perturbation current can generate the aforementioned 0.1% perturbation level up to the flux-surface $\psi \simeq 0.5$, which is better than in the TEXTOR case despite the size of ITER. Although the relative perturbation strength is similar, the perturbed structure corresponding to the various configurations is very different. As expected, the $n = 9$ configurations do not achieve much ergodization, the generated islands are very thin. Islands created by lower mode-number perturbations are considerably larger. Most of the $n = 3$ configurations perform much better, but those also differ largely from each other. The reason for this is the different alignment of the current structures with respect to the unperturbed field lines. This also underlines the importance of 3D calculations as opposed to estimates based solely on the relative perturbation strength $\delta B/B$.
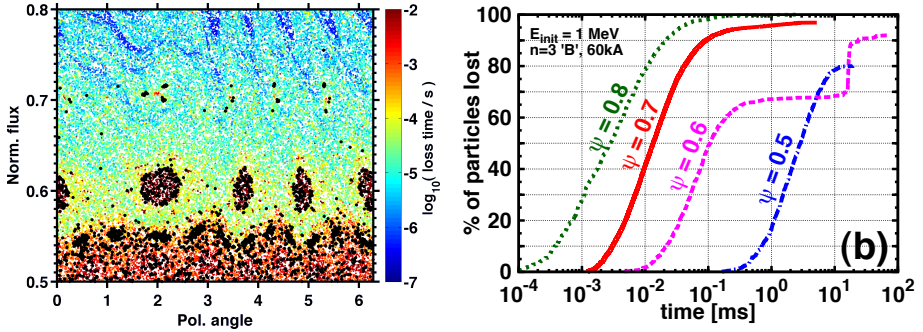
Figure 3.4: Case $n = 3$ "B". (a) Loss time of particles as a function of starting position $(\psi,\vartheta;\phi = 0)$. (b) Particle losses starting from different flux surfaces. Note that these figures differ from their counterparts in Paper C, see the errata for details.

In Paper C we aimed at better understanding the governing mechanisms of RMP induced fast electron transport. In the perturbed case the ergodic zone arising at the edge causes losses several orders of magnitude faster than in the unperturbed case. Without perturbations it takes $\mathcal{O}(10)$ ms until the losses initiate due to the drift orbit shift associated with the energy gain, at which point the runaways already have more than 10 MeV energy. Figure 3.4a shows a plot of the loss times in the flux coordinate system of (ϑ,ψ). To obtain this picture test particles were launched in the $n = 3$ "B" configuration at the same toroidal angle of $\phi = 0$ in the radial belt between $\psi = 0.5 - 0.8$. The flux coordinates were determined from the unperturbed equilibrium, where $\vartheta = 0$ marks the divertor, $\vartheta = \pi/2$ is the low field side midplane. Each particle is represented at its starting position by a color that shows the loss time associated with that particular starting position (note the logarithmic color scale). This picture allows us to study the ergodic magnetic field structure from a particle *loss* point of view. Due to the chaotic nature of field lines in the ergodic zone close to the LCFS slight changes of the individual particle starting positions can lead to orders of magnitude differences between the loss times for those particular particles. The chaotic structure on figure 3.4a is dominated by partially or completely broken magnetic islands at around $\psi = 0.5$ ($m/n = 7/6$), $\psi = 0.55$ ($m/n = 11/9$), $\psi = 0.6$ ($m/n = 4/3$) and $\psi = 0.7$ ($m/n = 5/3$). Black dots represent particles that are not lost during the 100 ms simulation time - these particles are confined within the KAM zones around the O points of remnant islands or whitheld by cantori [122] even at the

possible maximum energy reachable by the runaways in this scenario. Figure 3.4b shows the loss time distribution for particles launched at individual flux surfaces. The particle losses follow an exponential time evolution. The total final loss fraction, the start time of the losses and the characteristic loss rate all depend on the initial radial position ψ_0. For example, every $\Delta\psi_0 = 0.1$ step inside leads to about an order of magnitude longer loss initiation time and the characteristic loss rate also scales accordingly. It is interesting to note that the saturation for particles launched at $\psi = 0.6$ occurs around 70%, as the rest is confined within the remnant $4/3$ island at low energies. However, when their energy saturates, also these particles lose their confinement due to confinement volume shrinkage. This is what leads to the sudden increase in the losses between 10–20 ms. The confinement within the remnant $4/3$ O points of the particles launched at $\psi = 0.6$ is the reason why a higher loss fraction can be achieved by particles launched at $\psi = 0.5$ at a certain time ($t \simeq 5$ ms) as these are able to pass through the $4/3$ island at the ergodic regions surrounding the X-points. The timescales on figure 3.4b represent 2-4 orders of magnitude faster losses than in the unperturbed case. Most of the particles outside $\psi = 0.55$ are lost during the very early phases of the evolution, which can be favourable from the avalanche generation point of view. This also means that the particles lost due to RMP will have negligible energy gain.

However, losing fast electrons from the edge may lead to a larger inductive field in the centre of the plasma, making the runaway generation stronger there. Therefore, quantitative conclusions about the magnitude of the total runaway current can only be drawn from simulations where both the evolution of the electric field and losses due to RMP are included self-consistently. This could be achieved e.g. by the GO code (see section 3.6), using the results presented in Paper C as inputs, possibly in a form of radial transport coefficients and/or time-dependent losses at the edge.

Possible heat load anisotropies

Without RMP, in an *ideal case*, the RE losses would be isotropic in the toroidal direction, and located at the low field side due to the energy gain related outward shift of the drift surfaces with respect to the flux surfaces. The application of the RMP introduces an anisotropy in the mesh exit points correlated with the perturbation pattern, as will be discussed briefly in this subsection.
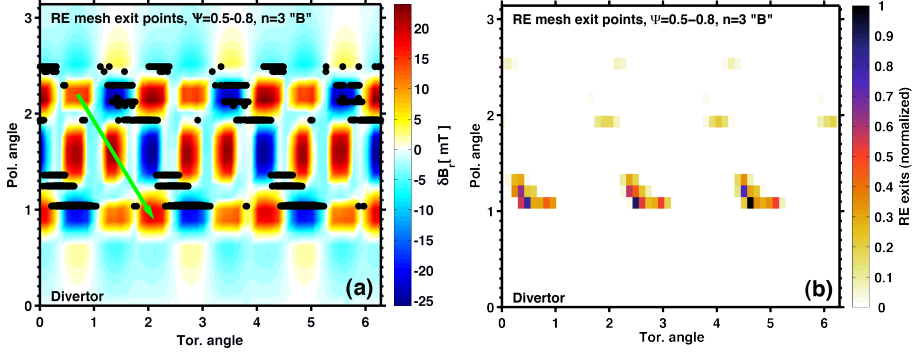
Figure 3.5: (a) Mesh exit points (black dots) overlaid on the radial perturbation strength δB_r. Particles get lost after passing regions where the field perturbation component points *inwards* (green arrow marks the particle passing direction). (b) 2D histogram of the mesh exit points at the LCFS.

The exit point pattern for case $n = 3$ "B" is shown in figure 3.5a-b in the (ϕ,ϑ) flux coordinate system at the LCFS. In figure 3.5a black dots mark the mesh exit points, overlaid on the local radial magnetic field perturbation component δB_r at the LCFS shown by the colormap, which is positive if δB_r points outwards. Figure 3.5b shows a 2D angular histogram of the mesh exits. The majority of the exit points are situated below the midplane $\vartheta < \pi/2$. Exit points are concentrated in the regions where the magnetic field perturbation component points inwards. The loss pattern follows the natural periodicity and helicity of the configuration, as we have shown for the $n = 3$ and seen for the $n = 9$ cases. Similar observations were reported for ripple induced losses as well [123–126]. This also means that although RMP scenarios with low n remove particles faster, but the heat loads may be more localized, especially in the presence of dominant 3D wall structures that can act as natural hot spots [127, 128]. The $n = 3$ configurations seem to provide a good runaway removal from the edge with the disadvantage of possible localised losses. However, this might be handled with properly positioning the RMP current pattern – the details, again, depend on the 3D wall shape. Rotation of the current pattern during a disruption can only offer possible aid in smoothing the RMP induced pattern if the rotation period is in the same order of the losses, that is in the order of milliseconds.

Transport in the perturbed field

We have found an almost perfect correlation between the particle radial steps and the local radial perturbation magnetic field $-\delta B_r$. The sign depends on runaway propagation with respect to the magnetic field, which in the ITER case is antiparallel. The particles follow a helical path passing in front of three consecutive RMP coils, which cause δB_r with different signs depending on the current direction, and therefore lead to either inwards or outwards radial steps. However, these radial steps bring the particles to a region with a different q. Hence, in the next round the angle of approach to the RMP pattern is different. This leads to a chaotic walk in the sense that the particle "walks" both along the orbit $(v_\parallel)$ and in the radial direction. Meanwhile, the alignment angle of the orbit to the 2D RMP pattern is constantly changing. The step sizes and the whole walk itself is deterministic but depend nonlinearly on the initial parameters.
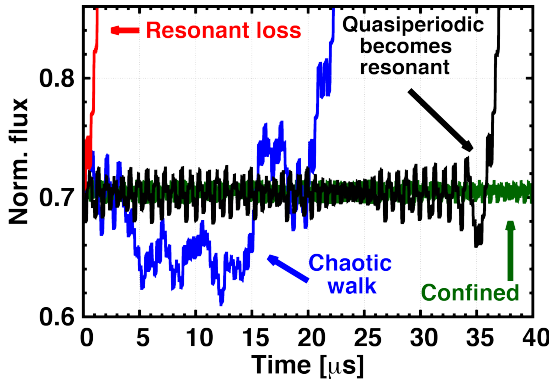

Figure 3.6: Four different types of typical particle behaviour: fast resonant loss, chaotic walk with and without quasiperiodic stage, confined.

Figure 3.6 shows examples of typical particle behaviour during the RMP governed chaotic walk process. The particles that are born in a resonant loss region where the consecutive steps lead to a sudden loss will get lost. Those particles for which the perturbation is averaged out along the orbit are the ones that become confined in the remnant O-points, undergoing a quasi-periodic oscillation in the radial direction. All the rest follows the chaotic walk, which leads to an anomalous diffusion process that explains the exponential dependence of the cumulative losses on time. Note that the lost particles can also undergo quasiperiodic phases, or move significantly inwards before finally moving out.

The most probable spot to exit the mesh is close to the end of the regions with many consecutive outwards steps, that is along the negative B_r fields. In figure 3.5a, shown with a green arrow, the particles move from the top left corner to the bottom right corner, that causes the losses to be more pronounced at the lower coils.
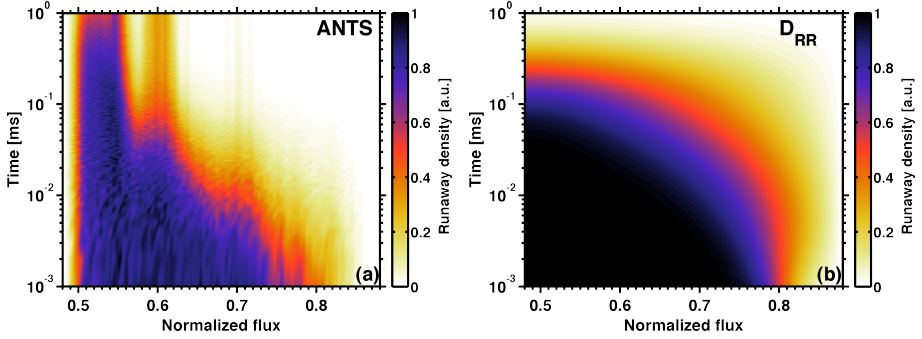

Figure 3.7: Time evolution of the RE density profile in the perturbed field calculated with (a) ANTS (b) Rechester-Rosenbluth diffusion.

In order to better understand the transport of the runaway ensemble under RMP, figure 3.7a illustrates the time evolution of the runaway density profile in the ITER $n = 3$ "B" configuration, as calculated by ANTS. The initial density profile was a flat-top between $\psi = 0.5 - 0.8$, and zero otherwise. Note the logarithmic time axis. Figure 3.7a demonstrates the exponential dependence of the loss initiation time on initial radial position as well as the exponential time dependence of the losses. We can also clearly observe particles trapped within remnant islands. Although the individual particle orbits are chaotic, the ensemble behaviour is reasonably smooth. This is very promising if we want to include the RMP induced transport in a simplified, e.g. 1D modelling, which is valuable if we aim to calculate the effect of RMP on runaway electron dynamics with a self-consistent electric field. For comparison, figure 3.7b shows the evolution with the same initial parameters calculated with the Rechester-Rosenbluth (RR) diffusion. There is a clear discrepancy between the two. Not only that the RR diffusion does not account for particle trapping, it also shows a different time- and ψ dependence. *However*, for the particles outside the remnant islands the characteristic loss time is in the same order as the ANTS result. This shows that although the RR diffusion is not sophisticated enough to describe the total transport process, it is still reasonable for order of magnitude estimates.

3.6 Runaway electron simulations with self-consistent electric field

In this section, we describe a model for self-consistent runaway electron generation calculations. This numerical tool, called the GO code, has been in development since several years [83, 86, 129, 130]. GO is the basis of the $E_\phi(\psi, t)$ electric field calculations for the ANTS simulations in Papers B & C. We show the effect of different impurities on runaway generation with an example from the JET tokamak and will also demonstrate the influence of magnetic perturbation induced radial transport of fast electrons on the whole process.

The GO code

The time evolution of the current density profile is determined by the runaway electron generation and the diffusion of the electric field governed by the parallel component of the induction equation

$$\frac{1}{r}\frac{\partial}{\partial r}\left(r\frac{\partial E}{\partial r}\right) = \mu_0 \frac{\partial}{\partial t}(\sigma_\parallel E + n_{\rm r}ec), \tag{3.7}$$

where $n_{\rm r}$ is the number density of the runaways – travelling with approximately the speed of light – and $\sigma_\parallel$ is the Spitzer conductivity with a neoclassical correction [7]. The changes of the (3.7) electric field are mainly determined by the short time scale changes of the conductivity, which strongly depends on temperature ($\sigma \propto T^{3/2}$). The model also includes a conducting plasma vessel [83, 129] but neglects coupling to the coils. The primary generation is calculated via the Dreicer process

$$\left(\frac{{\rm d}n_{\rm r}}{{\rm d}t}\right)_{\rm D} \simeq \frac{n_{\rm e}}{\tau}\left(\frac{m_{\rm e}c^2}{2T_{\rm e}}\right)^{3/2}\left(\frac{E_{\rm D}}{E}\right)^{3(1+Z_{\rm eff})/16} e^{-\frac{E_{\rm D}}{4E} - \sqrt{\frac{(1+Z_{\rm eff})E_{\rm D}}{E}}}.$$

Here, $E_{\rm D}$ is the (3.5) Dreicer field, and τ is the relativistic electron collision time $\tau = 4\pi\varepsilon_0^2 m_{\rm e}^2 c^3/(n_{\rm e}e^4 \ln\Lambda)$. The seed runaways are amplified via avalanching [16]:

$$\left(\frac{{\rm d}n_{\rm r}}{{\rm d}t}\right)_{\rm avalanche} \simeq n_{\rm r}\frac{E/E_{\rm c} - 1}{\tau \ln\Lambda}\sqrt{\frac{\pi\varphi}{3(Z_{\rm eff}+5)}}\times$$
$$\times\left(1 - \frac{E_{\rm c}}{E} + \frac{4\pi(Z_{\rm eff}+1)^2}{3\varphi(Z_{\rm eff}+5)(E^2/E_{\rm c}^2 + 4/\varphi^2 - 1)}\right)^{-1/2},$$

where E_c is the (3.6) critical electric field, $\varphi = (1 + 1.46\epsilon^{1/2} + 1.72\epsilon)^{-1}$ and $\epsilon = r/R$ denotes the inverse aspect ratio. In Paper D, we considered radial diffusion due to magnetic perturbations using the Rechester-Rosenbluth diffusion estimate [84] $D_{\mathrm{RR}} = \pi q v_\parallel R \left(\delta B/B\right)^2$, where $v_\parallel \simeq c$ is the parallel velocity, R is the major radius and $\delta B/B$ is the normalized magnetic perturbation amplitude. In the version of the GO code used in Paper D, the Dreicer and avalanche runaway rates and radial losses due to magnetic field perturbations are coupled to the evolution of the electric field through equation (3.7). Hot tail generation is efficient if the cooling rate is comparable to the collision frequency [131] and has been predicted to be important in ITER disruptions [76], but in the cases studied in this thesis, the cooling times are long enough for the Dreicer generation to dominate over hot-tail generation.

The GO code requires specification of the neutral impurity density as function of time and radius, $n_{\mathrm{Z}_i}^0(r, t)$. The time evolution is often assumed to be an exponential ramp-up, with a characteristic time on the ms timescale in agreement with numerical modelling [114]. The temperature and density evolution is modeled separately for each plasma component – electrons and Z_i ions. The energy balance equations describing the temperature evolution are

$$\frac{3}{2}\frac{\partial(n_{\mathrm{e}}T_{\mathrm{e}})}{\partial t} = \frac{3n_{\mathrm{e}}}{2r}\frac{\partial}{\partial r}\left(\chi r \frac{\partial T_{\mathrm{e}}}{\partial r}\right) + P_{\mathrm{OH}} - P_{\mathrm{line}} - P_{\mathrm{Br}} - P_{\mathrm{ion}} + \sum_i P_{\mathrm{c}}^{\mathrm{eZ}_i},$$

$$\frac{3}{2}\frac{\partial(n_{\mathrm{Z}_i}T_{\mathrm{Z}_i})}{\partial t} = \frac{3n_{\mathrm{Z}_i}}{2r}\frac{\partial}{\partial r}\left(\chi r \frac{\partial T_{\mathrm{Z}_i}}{\partial r}\right) + P_{\mathrm{c}}^{\mathrm{Z}_i\mathrm{e}} + \sum_{j \neq i} P_{\mathrm{c}}^{\mathrm{Z}_i\mathrm{Z}_j}. \tag{3.8}$$

Here $P_{\mathrm{OH}} = \sigma_\parallel E^2$ is the Ohmic heating power density, P_{line} and P_{Br} are the line- and Bremsstrahlung radiation and P_{ion} is the ionization energy loss. Bremsstrahlung losses are taken into account with the formula $P_{\mathrm{Br}} = 1.69 \cdot 10^{-38} n_{\mathrm{e}}^2 \sqrt{T} Z_{\mathrm{eff}}$ [132]. Due to the different collision times the different species are modeled separately. The (3.8) energy balance equations are coupled with collisional energy exchange terms between Maxwellian species [14]: $P_{\mathrm{c}}^{ij} = 3n_i(T_j - T_i)/2\tau_{ij}$ with the heat exchange time

$$\tau_{ij} = \frac{3\sqrt{2}\pi^{3/2}\epsilon_0^2 m_i m_j}{n_j e^4 Z_i^2 Z_j^2 \ln\Lambda}\left(\frac{T_i}{m_i} + \frac{T_j}{m_j}\right)^{3/2},$$

where the subscripts i, j now refer to electrons as well as deuterium & impurity ions. The heat diffusion coefficient is assumed to be constant ($\chi = 1$ m^2/s) unless otherwise indicated. Studies were made in ref. [83]

to test the influence of this assumption on the GO simulation results. Radiation has the strongest cooling effect on the electrons. To describe the line radiation we calculate the ionization of the impurities by calculating the density of each charge state for every ion species ($n_{Z_i}^k, k = 0..Z_i$):

$$\frac{\mathrm{d}n_{Z_i}^k}{\mathrm{d}t} = n_\mathrm{e} \left(I_{k-1}n_{Z_i}^{k-1} - (I_k + R_k)n_{Z_i}^k + R_{k+1}n_{Z_i}^{k+1} \right),$$

where I_k denotes the electron impact ionization rate for the k-th charge state and R_k is the radiative recombination rate [132]. The line radiation is calculated by

$$P_\mathrm{line} = \sum_i n_{Z_i}n_\mathrm{e}L_{Z_i}(n_\mathrm{e}, T_\mathrm{e}).$$

The radiation rates $L_{Z_i}(n_\mathrm{e}, T_\mathrm{e})$ are extracted from the ADAS database [133]. We note that from a numerical point of view this ionisation / recombination & radiation calculation is the most CPU intensive task as each transition for every charge state in every ion species has to be calculated in every time step. Including impurities in the calculation therefore increases the required CPU time by a factor of $10^2 - 10^3$.

The effect of ITER-like wall in JET

Runaway electrons with energies of several MeVs are routinely observed during disruptions in JET [64, 134–138]. One of the open questions, which is the main topic of Paper D, is the observed different runaway behaviour in the presence of carbon and beryllium wall impurities, a question which recently gained interest in the view of the new ITER-like wall (ILW) installed at JET. The ILW comprises solid beryllium limiters and a combination of bulk tungsten and tungsten-coated carbon fibre composite divertor tiles [139].

The ILW has a significant impact on disruption physics in general [66, 140]. One of the major differences compared to disruptions with the carbon wall is that a lower fraction of energy is radiated during the disruption process, yielding higher plasma temperatures after the thermal quench. This will in turn affect the runaway formation. Drawing experimental conclusions at present time is difficult due to the limited number of runaway experiments carried out with the ILW so far. The aim of Paper D was to perform a comparative modelling study of two similar L-mode limiter discharges, performed with different wall materials to provide a deeper insight in the differences. In both cases the

disruption was induced by slow argon injection. In the CFC case the thermal quench is quick, which gives rise to runaways with a significant current plateau. In the ILW case the thermal quench lasts for about 80 ms and results in only a negligible amount of runaways. As the result of relatively low plasma density coupled with increased wall sputtering in L-mode, these discharges have substantial steady state wall impurity content. However, the level of impurity sputtering during the disruption is unknown and therefore a scan for the impurity amounts was necessary. The argon content can be estimated based on the total injected argon amount with a reasonable assumption for the mixing efficiency [141].

We found that in general the runaway current increases with argon content, while it decreases with carbon/beryllium content. The differences are due to the nonlinear nature of the simulations that amplify the differences in the initial temperature- and density profiles, injected argon amount and the presence of different background impurities, all of which amplify each others' effect. The presence of beryllium effectively reduces the runaway current at argon contents of experimental relevance. As low as 10% beryllium leads to a factor of two decrease in runaway current. The presence of impurities also decreases the relative fraction of primary runaways. Beryllium increases the avalanche *fraction* more than carbon, that can be useful as the characteristic growth rate of avalanche is an order of magnitude lower than for Dreicer generation. This means that intrinsic and/or active runaway mitigation mechanisms have more time to have an effect. In Paper D the experimentally measured runaway currents were reproduced at reasonable impurity contents. The simulations indicate that the runaway current and Dreicer fraction reducing effect of the wall impurities decreases with increasing Ar content (for the plasma parameters in these shots) and the behaviour is comparable above 50% argon content. This suggests that runaway electrons will probably return in future experiments regardless of the ILW when argon is used in large quantities in massive gas injection (MGI) experiments on JET as well as ITER.

The effect of runaway diffusion

As we have described earlier in this thesis, magnetic perturbations can lead to increased radial runaway transport. In general, magnetic perturbations can come from the RMPs, MHD mixing, error fields, the response of the control system to the disruption, instabilities enhanced by the gradients during runaway evolution, etc. In Paper D we use

the aforementioned Rechester-Rosenbluth diffusion [84] to demonstrate the effect of magnetic perturbations on runaway current evolution. The magnetic perturbations are kept constant in space and time as this is sufficient to demonstrate the effect and only requires one free parameter, $\delta B/B$. For simplicity, the evolution of the main plasma parameters such as temperature is taken from the experimental data. Although the radial transport is not as sophisticated as in the ANTS simulations, the electric field and runaway generation is calculated self-consistently.

Without runaway losses due to magnetic perturbations, the simulations end with a considerable runaway current in both shots, although its value is higher in the C wall case than in the ILW case. The current evolution is best matched with the experiment at a perturbation level of $\delta B/B = \mathcal{O}(10^{-3})$. With a constant perturbation the runaway plateau cannot be reproduced, but otherwise the main features of the current evolution (such as the current decay rate) are similar. With a perturbation level of $\delta B/B = 10^{-3}$ the runaway redistribution rate is comparable to the generation rate and the runaways spread out in the plasma before they can form a strong runaway population. Even if the runaways are not completely removed, the runaway current *density* is decreased which in turn decreases the avalanche generation rate. We found that the maximum value of the runaway current drops exponentially as a function of $\delta B/B$ for both cases, but the percentages reached are significantly different for the two walls cases. The reason why the ILW case is more sensitive to the losses due to magnetic perturbations than the C wall case in the simulations is that in the C wall case the Dreicer mechanism is significantly stronger, generating a higher fraction of the runaway current than in the ILW case. The Dreicer generation has approximately an order of magnitude shorter characteristic rise time than the avalanche mechanism, and therefore the losses due to radial diffusion (as well as other loss mechanisms) can more easily counteract the runaway growth if the Dreicer current fraction is low.

4 | Sawtooth instability

The sawtooth oscillation is a periodic collapse phenomenon widely observed in tokamaks [7]. It develops in the plasma core when the safety factor on-axis (q_0) is below 1. In the core, the temperature and density ramp up slowly over most of the sawtooth period while they rapidly *crash* down in the remainder, as illustrated in figure 4.1. During the
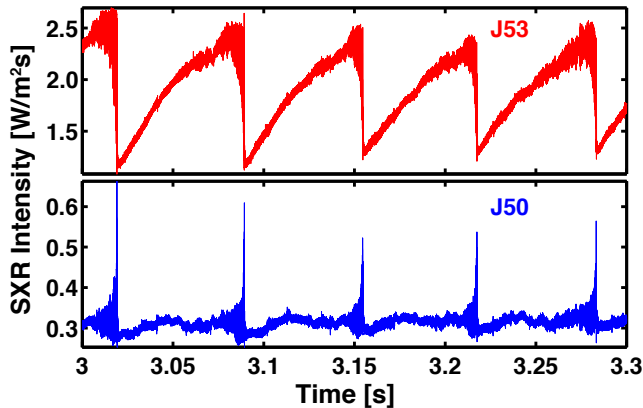

Figure 4.1: Sketch of a central (J53) and non-central (J50) SXR channel during five sawtooth crashes in ASDEX Upgrade shot #20975.

crash phase there is an intensive density- and heat transport outwards. The temperature and density outside the core ramp up quickly just after the crash, and decrease gradually to their equilibrium value. This effect is most noticeable on the line integrated Soft X-Ray (SXR) measurements of the plasma core, where the repeating sequence of slow growth and sudden drop of intensity gives the characteristic sawtooth shape [32].

The *measured* SXR intensity depends mainly on the electron density and temperature $I_{\text{det}} \propto n_{\text{e}}^2 T_{\text{e}}$ [142, 143], that makes it a preferred tool for the investigation of sawteeth. The sawtooth phenomenon is important for various reasons. The plasma can survive the performance-reducing drops of the main core plasma parameters, but the coupling of sawteeth to other, more harmful modes [29, 30] can result in a substantial confinement degradation. Sawteeth might also pose a threat to plasma self-heating [18]. On the other hand, the sawtooth instability will remove helium ash and impurities from the core of burning plasmas, thereby preventing the degradation of the core temperature [28]. Thus the goal is to control the sawteeth, not to totally avoid them. For these reasons, significant effort has been placed by the fusion community in observing, controlling and understanding the sawtooth instability.

Ever since the first observation [32], sawteeth have been connected to the $(1,1)$ internal kink mode [7], which is a well-known sawtooth precursor. It is characterized by an $(m,n) = (1,1)$ spatial structure, where m and n are the poloidal and toroidal mode numbers, respectively ($q_0 < 1$ implies the existence of a $q = 1$ surface). Most of the sawtooth control methods rely on influencing the $(1,1)$ internal kink mode, that can be realized with a variety of heating and current drive techniques [144–149]. The knowledge of how to control sawteeth has improved significantly in recent years [31, 150], however, the physical processes that govern sawtooth oscillations remain not fully understood.

For example, the details of the crash mechanism itself still need to be revealed. Kadomtsev was the first to come up with a model [151] that was successful at explaining the characteristic timescales, but fails to explain e.g. the evolution of the q profile. Throughout the years there have always been models which later on have been contradicted with more and more detailed experimental observations. The importance of higher order harmonics of $(1,1)$ has recently been investigated on ASDEX Upgrade [55–57] and HT-7 [152]. It has been proposed that the interaction of the $(1,1)$ kink and higher order harmonics can lead to a stochastization of the plasma core. These results fit well into the stochastic model [153, 154] of the sawtooth crash. The stochastic model proposes the formation of a broad ergodic zone in the vicinity of the $q = 1$ surface that causes the collapse. The exact generation mechanism of such an ergodic zone, however, is yet unknown.

Careful analysis of the precursor phase on ASDEX Upgrade [33–35] and HT-7 [36] showed, that a low frequency signal component is visible on the central SXR signals, and it gains energy just before the sawtooth crash. Observations of a second, lower amplitude and lower frequency $n = 1$ mode have also been reported on JET [37]. This signal component is called the **Low Frequency Sawtooth Precursor (LFSP).** The existence of this low frequency mode and its possible interaction with the internal kink fits well into the stochastic model [33], and can be a key element in the understanding of the crash mechanism. Paper F focuses on the detailed analysis of the data from the central soft X-ray channels of ASDEX Upgrade [155] in order to better understand the behaviour of the LFSP, and the connection between it and other sawtooth precursor modes. The line of sights for the SXR cameras are shown in figure 4.2.
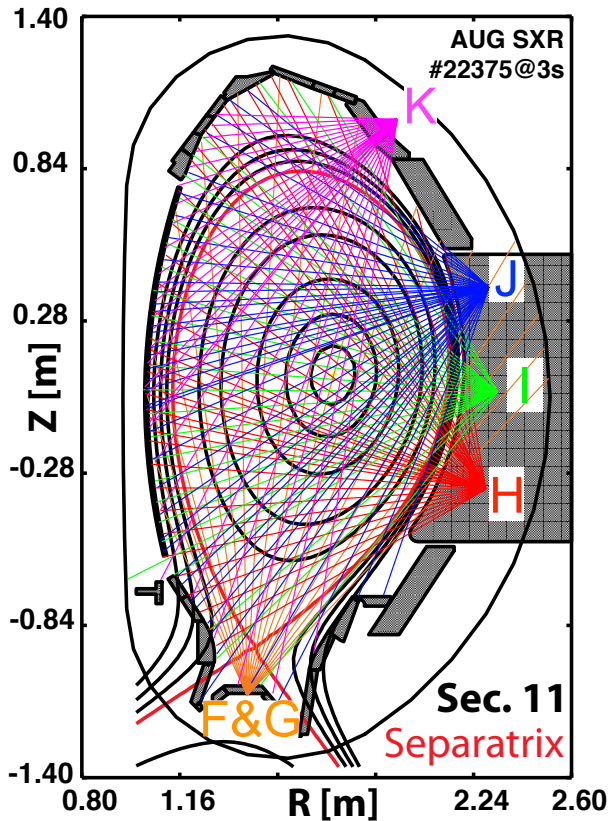

Figure 4.2: The line of sights of the SXR cameras F–K of ASDEX Upgrade.

4.1 Experimental investigation

Time-frequency evolution

Most of the analysis tools used in Paper F are based on linear continuous time-frequency transforms such as the Short Time Fourier Transform (STFT) and the Continuous Wavelet Transform (CWT) [156]. Continuous transforms have the advantage of being time-shift invariant that is crucial in transient signal analysis. By using linear transforms we are able to calculate the power distribution of the signal over the time-frequency plane called the **spectrogram** (in case of using STFT) that is used to visualise the time-frequency evolution of signal components. The spectrograms have shown the existence of the LFSP 20–40 ms before the sawtooth crash in a wide variety of shots. The LFSP was investigated during different heating- and active sawtooth control schemes, and was observable in all cases with a similar time-frequency structure. The main phenomena [34, 35] also proved to be the same in different shots from year to year. These observations support the generality of the LFSP. In order to improve event statistics in various techniques – for example, correlation analysis – we required statistical averaging over several similarly behaving sawtooth crashes. The spectrograms allow to follow the complex time-frequency evolution that served as a basis of finding similar crashes for the averaging.

The frequency ratio of the (1,1) and the LFSP had to be estimated with a quantitative method. For this we used a global **ridge following algorithm** based on graph theory, inspired by P. Varela [157]. In this method the spectrogram is represented as a graph: the nodes mark the time-frequency points, and edges connect each node at a given time point i with all the nodes in the following time point $i+1$: $x_{i,j} \rightarrow x_{i+1,k}$ $k = 1 \ldots N$ for $\forall\, i,j$, where i and j are the time- and frequency indexes, respectively. The edges are weighted with a scheme that takes the strength of each point and their difference in frequency into account in a way that is optimized for the actual signal-to-noise ratios. The shortest path in this weighted graph represents the frequency evolution of the signal component of interest. The path is calculated with a modified version of Dijkstra's shortest path algorithm [158]. The frequency ratio of the two modes does not show any particular temporal development pattern, it is restricted to the 0.5–0.7 range, and seems not to equal any specific low order rational.

The spectrograms show that the LFSP is a low energy mode during most of the precursor phase, but it swiftly gains energy right before the sawtooth crash. In order to quantitatively characterize the power evolution of the LFSP, we estimated the **bandpower** of the frequency range associated with it. This is done by integrating the spectrogram in frequency over a given frequency range [159]. The estimated bandpower then serves as an input for other analysis methods. We have to note that the bandpowers and the power modulation acquired with the ridge following algorithm show good agreement with each other, but the bandpower is more preferred for its simpler algorithm and also requires lower computational effort.

For quantitative description of the time evolution of the energy and to estimate the growth rate of the LFSP we fitted exponential curves to the bandpowers of the LFSP for the investigated sawtooth crashes in the precursor phase. We calculated the weighted average of the fitted parameters (maximal bandpower, growth rate, background noise) in the aforementioned crash groups. The parameters show good agreement between the different shots, consequently the ramp-up of the LFSP is very uniform from the amplitude growth point of view. The average amplitude growth rate is $\gamma_A = (407 \text{ s}^{-1} \pm 3\%)$, that suggests that the LFSP is most probably a resistive MHD mode [160]. These observations can be the basis to extract the critical values of the underlying parameters such as the LFSP amplitude necessary for the crash, as will be discussed in section 4.2.

Mode interaction

Investigating the possible interaction of the LFSP and the (1,1) mode is crucial in order to understand the origin of the LFSP and its role in the sawtooth crash. One way to characterize the interaction of different modes is the **bandpower correlation** method [159] in which the bandpowers of LFSP and (1,1) are correlated with each other. Our previous results have already shown an interaction between these two modes in the early precursor phase before the crash [34]. In Paper F we extended the previous investigation to improve the event statistics by averaging the bandpower correlation functions for several crashes with similar behaviour. We found that a $> 50\%$ correlation can systematically be found for a wide range of shotnumbers, that implies a connection between the two modes long before the crash. Bandpower-correlation also provided a way to determine the location in which the two modes are interacting,

that is also visible slightly outside the inversion radius, the importance of which will be described in section 4.2.

The other method employed in the analysis is **bicoherence**, that is able to measure phase coupling between signal components [161]. Despite the low energy of the LFSP, we found a significant, 60% bicoherence between the (1,1) and the LFSP already 15 ms before the crash event. This suggests the existence of a nonlinear interaction between the two modes in the early, low-energy phase of the LFSP, in agreement with the bandpower correlation analysis.

Spatial structure

The spatial structure of the LFSP is a key issue in understanding the phenomenon, but one has to overcome the difficulties raising in the detection and mode number estimation of a low energy, transient core mode. The only diagnostics available on ASDEX-Upgrade – at the time of investigation – that have the required spatiotemporal resolution of the plasma core are the soft X-ray cameras, for which we have applied previously developed wavelet based methods for detecting short-lived plasma eigenmodes and determining their spatial structure [162, 163]. A typical model structure for an MHD eigenmode is

$$B(\psi, \theta, \phi, t) = B(\psi)e^{i\omega t}e^{i(m\theta + n\phi)},$$

that defines the (m, n) mode numbers. Therefore, we can determine the mode number if we measure the phase of a given ω frequency mode at different spatial positions. Our mode number determination is based on the phase of the continuous analytical wavelet transform [156]. For each (u, ξ) point of the time-frequency plane, $\vartheta_{x,y}(u, \xi)$ relative phases between all (x, y) pairs of signals are calculated. For a pure harmonic structure, these relative phases would lie on a straight line as a function of the $\phi_{x,y}$ relative probe position as illustrated in figure 4.3. The slope of the best fitting straight line gives the mode number with the residual defined as:

$$\mathcal{Q}_l(u, \xi) = \sum_{x,y} \|\vartheta_{x,y}(u, \xi) - l \cdot \phi_{x,y}\|^2_{2\pi},$$

where $l = \{m, n\}$ is the toroidal or poloidal mode number and $\|\ldots\|_{2\pi}$ is the norm by taking the optimum shift of $\vartheta_{x,y}$ by $2\pi z$, $z \in \mathbb{Z}$. This method gives a best fitting mode number for each point on the time-frequency plane, that allows one to follow the time-frequency evolution
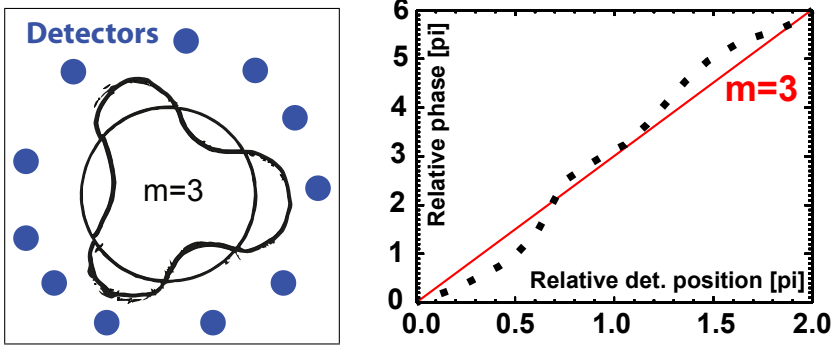
Figure 4.3: (a): Illustration of an $m = 3$ mode surrounded by an array of probes, picking up different phases of the oscillation. (b) $\vartheta_{x,y}$ relative phases as a function of $\phi_{x,y}$ relative probe positions. The slope of the curve gives the most fitting mode number.

of the mode numbers. However, mode numbers are a relevant quantity only in limited regions, where coherent modes exist. We can find these regions based on a criterion for the $\min_l\{\mathcal{Q}_l(u,\xi)\}$ values, or on wavelet minimum coherence [162], or on the combination of both, as in Paper F.

With the right choice of $\phi_{x,y}$, the mode number estimation can be applied for both toroidal and poloidal mode numbers. Toroidal mode numbers were estimated using two identical SXR cameras placed 135° apart toroidally but having the same lines of sight in the poloidal cross-section. Up to 4 central channel pairs inside the sawtooth inversion radius were used for mode number estimation. For the poloidal mode numbers we had to select lines of sight in the same toroidal cross-section that were tangential to approximately the same flux surface and measured high bandpower values on the mode frequency. The mode structure distortion (caused by toroidal effects and the magnetic field gradient) can be compensated if we transform the inhomogeneous magnetic field to a homogeneous one by using a straight field line poloidal angle coordinate [164] instead of the geometrical coordinate.

According to these measurements, the mode number of the LFSP is (1,1), equal to the "classic" (1,1) kink mode. The significance of this result is discussed in section 4.2.

4.2 The possible role of the LFSP

Our knowledge on the LFSP and its role in the sawtooth crash is not yet sufficient for a clear theoretical understanding, nonetheless, we present a few possible ways how the LFSP can be fit into different sawtooth crash models.

If the (1,1) kink mode already exists in the plasma, it provides a strong periodic drive force that can excite other modes as well (directly via e.g. magnetic coupling; or indirectly through the change of the profiles [38]). The mode numbers of the LFSP were found to be identical to the (1,1) internal kink mode, this also means that the LFSP is located at the same radial position, at the $q = 1$ surface. These observations make the excitation of the LFSP by the (1,1) very likely via magnetic coupling, that is possible even if the frequency ratio is irrational [48]. A sign of this interaction is the measured bandpower crosscorrelation, and the high value of bicoherence.

It has already been shown that the (1,1) internal kink mixed with its upper harmonics can contribute to the stochastization of the plasma core [55, 56]. If we investigate the interaction of the (1,1) and the LFSP we observe that the additional small ($< 1\%$) perturbation with $f_{\mathrm{LFSP}} = 0.6 f_{(1,1)}$ mixed with the original (1,1) mode at the observed spatial position creates a relatively broad stochastic layer and an "opening" at the X point of the (1,1) island [165]. This is shown schematically in figure 4.4. The important factor in this stochastization is the frequency
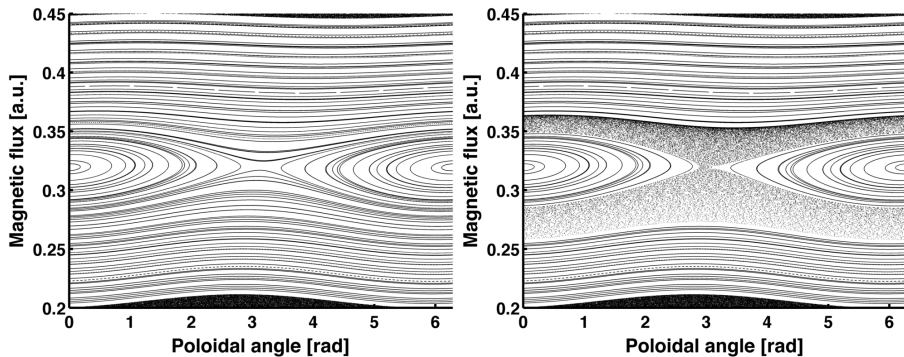

Figure 4.4: (a): Sketch of the magnetic island generation as a result of the (1,1) mode. (b): X point opens up and broader stochastic region appears due to the additional presence of the LFSP.

ratio and the identical spatial structure of the two coupled modes. The fact that the two modes are interacting also outside $q = 1$ enables the formation of an ergodic layer at the outer island separatrix. Adding upper harmonics does not open up the magnetic structure as effectively as the LFSP. The generation of a broad stochastic layer near the (1,1) island separatrix and especially at the X point coincides well with the 2D electron cyclotron emission (ECE) measurements of the crash phase [152, 166, 167]. As was discussed in chapter 2, small modifications in the perturbation amplitude can result in swift changes of the magnetic structure. It is probable that the ergodic zone visualized in figure 4.4 appears almost instantly when the LFSP reaches a certain critical amplitude, as was implied during the analysis of the power evolution. This could explain the sudden onset of the crash.

The implications of this model on the evolution of the q profile are consistent with the measurements, namely that the position of the $q = 1$ surface is preserved and that q on axis remains below unity. The interaction of the LFSP and the (1,1) kink implies a partial reconnection procedure that is consistent with the observations that heat comes out from the central core region through the X-point of the (1,1) island and the (1,1) island survives the crash [167]. The sudden onset of the crash, the rapidity of the temperature collapse and the incomplete relaxation of the current profile can also be explained by the interaction of modes with commensurate spatial structure [56].

An interesting question is why the two modes with equal spatial structure have different frequencies? One possible explanation is the difference of the mode types. According to the observed growth rate of $\gamma_A \sim 400$ s^{-1}, the LFSP is most probably a resistive mode [160]. On the other hand, the internal kink is often characterized as an ideal mode before the crash [168]. However, an ideal mode cannot be responsible for changes in the magnetic topology, while a resistive can be [169]. In the ASDEX Upgrade the presence of a (1,1) island is instantly visible after the crash, but not before [167]. These experimental observations cannot be described solely with ideal MHD theory.

As of today, we understand the LFSP as a secondary instability driven by the (1,1), that causes, or contributes to the crash. During the years, several different crash models have been proposed, each with experimental support [31]. The LFSP can play a role in the models that involve field line stochasticity, chaos or partial magnetic reconnection. There are indications that the sawtooth crash might be governed

by different mechanisms in the various devices [27], or by a mixture of the possible mechanisms. One of the latter is the possibility that the formation of an $(1,1)$ island or an ergodic layer around $q = 1$ provides a steep temperature gradient, that excites secondary ideal MHD instabilities during the crash [38], that would explain the rapidity of the temperature and density collapse. There is also the possibility that the LFSP is excited, driven or destabilized by the changes of the parameter profiles initiated by the (1,1) mode evolution. In the latter case the interaction of the reconnection process (that is enhanced by the presence of the LFSP) and the secondary instabilities is very complex and yet unclear. These questions cannot be answered without extensive MHD simulation studies. Either way, it seems very improbable that a crash model without partial magnetic reconnection can be consistent with all the experimental observations [38, 167], and as outlined above, the LFSP can play a crucial role in the reconnection process.

5 | Summary

Somewhere, something incredible is waiting to be known.
– Carl Sagan

The present thesis describes problems in the field of tokamak plasma physics related to the effect of magnetic perturbations on the tokamak magnetic structure. We have shown that magnetic perturbations can generate ergodic zones both in the core and at the plasma periphery. These ergodic zones significantly alter the radial transport due to the largely anisotropic transport in magnetized plasmas.

In the first part of the thesis, we aimed on utilizing this feature. The high energy population of runaway electrons that can form in disruptions poses a large threat to reactor-scale tokamaks like ITER, and the runaway generation has to be mitigated for a reliable operation. One possible option for runaway removal is to artificially generate ergodic zones in the post-disruption plasma by external resonant magnetic perturbation (RMP). The ergodic zones arising at the edge can lead to the removal of particles before they can reach large energies. Experimentally, the concept shows ambivalent results, showing success on several tokamaks, while lacking positive results on others. Numerical analysis is necessary to better understand the phenomenon.

In Paper A we focused on developing a numerical tool for the study of runaway electron drift orbits in 3D magnetic fields and understanding the experimental results measured on the TEXTOR tokamak. We found that runaway electrons in the core of the plasma are likely to be well confined. For low-energy ($\simeq 1$ MeV) particles closer to the boundary, the onset time of the losses is dependent on the amplitude of the magnetic perturbation, and this should affect the maximal runaway current. The runaway current damping rate is insensitive to the magnetic perturbation level, and its experimentally measured value is consistent with our simulations. We have also found that a significant loss of runaways

happens independently of the RMP, as a result of the confinement volume shrinkage at larger energies. We concluded that the experimental success of RMP on smaller devices can not be understood solely based on drift orbit simulations, but only if more complex effects such as e.g. MHD perturbations are taken into account as well.

In Paper B and Paper C we investigated the effectiveness of the proposed ITER RMP system. As expected, we found that runaways in the core ($\psi \lesssim 0.6$) are well confined. However, runaways are rapidly lost if $\delta B/B \gtrsim 10^{-3}$, which corresponds to the region outside the normalised flux $\psi \simeq 0.6$. The losses are caused partly by the confinement volume shrinkage and partly by the increased radial transport in the stochastic region. We performed simulations for several perturbation configurations and concluded that runaway losses are quite sensitive to the perturbation configuration. We identified one of the possible $n = 3$ perturbations to be the most efficient in this respect. We have identified the radial perturbation component δB_r as the main reason for particle radial "steps" and explored the chaotic processes governing the radial transport. We have also studied loss anisotropies arising from the usage of RMP. The results indicate that the presence of RMP not only increases the amount of lost particles, but may also influence the avalanche generation at the edge, since it leads to earlier losses of particles with lower energies. The actual effect of the RMP on the whole runaway electron population and dynamics can only be estimated with more complex simulations that take into account the electric field dynamics self-consistently.

In Paper D we studied runaway dynamics by using a tool that is capable of handling runaway generation with self-consistent electric field calculation, the GO code. This tool also includes modules to calculate the evolution of plasma parameters and impurity injection. We have shown that the difference observed in runaway behaviour on JET with two different wall materials (carbon, beryllium) can be explained with this relatively simple tool, but further studies are necessary for a more complete modelling. The results indicate that runaway electrons are expected to be present if massive gas injection is applied even with the ITER-like wall. In this paper we also demonstrated the effect of magnetic perturbations on the runaway current evolution with a self-consistent electric field. A perturbation in the range of $\mathcal{O}(10^{-3})$ is sufficient to counteract the avalanche mechanism and significantly alter the runaway dynamics.

In Paper E we have studied runaway positrons originating from runaway electrons in disruptions. These positrons can form in large numbers, gain relativistic energies and have a lifetime of seconds. We have calculated the distribution function of the positrons and estimated their detectability through synchrotron emission. Synchrotron spectra emitted by positrons, if measured, may offer information about the post-disruption plasma parameters.

Paper F is dedicated to the deeper understanding of the sawtooth crash mechanism, again on the basis of the perturbed magnetic structure. It presents a detailed analysis of the Low Frequency Sawtooth Precursor (LFSP) mode appearing at a slightly lower frequency than the well known sawtooth precursor (1,1) internal kink mode, as observed on the soft X-ray (SXR) diagnostic of the ASDEX Upgrade tokamak. A number of advanced data analysis methods were applied, such as the ridge following algorithm, bandpower-correlation, bicoherence for MHD modes, and a wavelet based method to determine core mode numbers on the time-frequency plane using SXR signals. Most of these techniques are new or have not been used in such a way before. The results indicate that the frequency of the LFSP is $0.5 - 0.7$ times the frequency of the $(1, 1)$ mode and has a growth rate of $\gamma_A \simeq 400$ s^{-1}, which is typical for a resistive core MHD mode. We have shown the correlation and phase coupling of the two modes in the early precursor phase. As was observed, the spatial structure of the LFSP agrees with that of the $(1, 1)$ kink and this enhances the possible interaction. It has been proposed that the interaction of the two modes with the same spatial structure but different frequency enhances the formation of a core ergodic zone. These results contribute to the sawtooth models involving field line stochasticity. Extensive simulation studies are required in order to better understand the LFSP and its role in the sawtooth crash in the future.

References

[1] United Nations. Report of the world commission on environment and development. General Assembly Resolution, **42** (1987), 187. http://www.un.org/documents/ga/res/42/ares42-187.htm.

[2] European Physical Society. Energy for the future - EPS position paper on the nuclear option. Press release of the European Physical Society, (2007), 1–24. http://nuclear.epsdivisions.org/highlights-1/energy-for-the-future-the-nuclear-option.

[3] Flakus, F.N., Cleveland, J.C. and Dolan, T.J. Nuclear fusion: Targeting safety and environmental goals. IAEA Bulletin, **37** (1995)(4), 22–25. http://www.iaea.org/Publications/Magazines/Bulletin/Bull374/37402042225.pdf.

[4] Cook, I. et al. Safety and environmental impact of fusion. Technical Report EFDA-S-RE-1, European Fusion Development Agreement, Garching bei München (2001). http://www.efda.org/eu_fusion_programme/downloads/scientific_and_technical_publications/SEIF_report_25Apr01.pdf.

[5] Chen, F.F. *An Indispensable Truth: How Fusion Power Can Save the Planet*. Springer (2011). http://dx.doi_notnow.org/10.1007/978-1-4419-7820-2.

[6] Dolan, T.J. *Fusion research*. Pergamon Press, corrected edition (2000).

[7] Wesson, J. *Tokamaks*. Clarendon Press, Oxford, third edition (2004). http://www.iop.org/EJ/abstract/0741-3335/46/3/173515.

[8] Freidberg, J. *Plasma Physics and Fusion Energy*. Cambridge University Press (2008).

[9] McCracken, G. and Stott, P. *Fusion: The energy of the Universe.* Elsevier Academic Press (2005).

[10] Weizsäcker, C.F. Zur Theorie der Kernmassen (On the theory of nuclear masses). Zeitschrift für Physik A Hadrons and Nuclei (Journal of Physics), **96** (1935), 431–458. http://dx.doi_notnow.org/10.1007/BF01337700.

[11] *All-the-World's Tokamaks.* www.tokamak.info.

[12] The ITER Team. Progress in the ITER Physics Basis. Nuclear Fusion, **47** (2007)(6). http://iopscience.iop.org/0029-5515/47/6.

[13] Dreicer, H. Electron and ion runaway in a fully ionized gas. I. Phys. Rev., **115** (1959)(2), 238–249. http://prola.aps.org/abstract/PR/v115/i2/p238_1.

[14] Helander, P. and Sigmar, D.J. *Collisional transport of magnetized plasmas.* Cambridge University Press, Cambridge (2002).

[15] Nygren, R. et al. Runaway electron damage to the Tore Supra phase III outboard pump limiter. Journal of Nuclear Materials, **241-243** (1997)(0), 522–527. http://www.sciencedirect.com/science/article/pii/S002231159780092X.

[16] Rosenbluth, M. and Putvinski, S. Theory for avalanche of runaway electrons in tokamaks. Nuclear Fusion, **37** (1997)(10), 1355. http://stacks.iop.org/0029-5515/37/i=10/a=I03.

[17] Shimada, M. et al. Progress in the ITER physics basis chapter 1: Overview and summary. Nuclear Fusion, **47** (2007)(6), S1. http://stacks.iop.org/0029-5515/47/i=6/a=S01.

[18] Hender, T. et al. Chapter 3: MHD stability, operational limits and disruptions. Nuclear Fusion, **47** (2007)(6), S128. http://iopscience.iop.org/0029-5515/47/6/S03/.

[19] Ghendrih, P., Grosman, A. and Capes, H. Theoretical and experimental investigations of stochastic boundaries in tokamaks. Plasma Physics and Controlled Fusion, **38** (1996)(10), 1653–1724. http://stacks.iop.org/0741-3335/38/1653.

[20] Yoshino, R. and Tokuda, S. Runaway electrons in magnetic turbulence and runaway current termination in tokamak discharges. Nuclear Fusion, **40** (2000)(7), 1293–1309. http://stacks.iop.org/0029-5515/40/1293.

[21] Finken, K. et al. Losses of runaway electrons during ergodization. Nuclear Fusion, **46** (2006)(4), S139–S144. http://stacks.iop.org/0029-5515/46/S139.

[22] Finken, K. et al. Runaway losses in ergodized plasmas. Nuclear Fusion, **47** (2007)(2), 91–102. http://stacks.iop.org/0029-5515/47/91.

[23] Lehnen, M. et al. Suppression of runaway electrons by resonant magnetic perturbations in TEXTOR disruptions. Physical Review Letters, **100** (2008)(25), 255003. http://prl.aps.org/abstract/PRL/v100/i25/e255003.

[24] Lehnen, M. et al. Runaway generation during disruptions in JET and TEXTOR. Journal of Nuclear Materials, **390-391** (2009), 740 – 746. http://www.sciencedirect.com/science/article/B6TXN-4VFK84W-2H/2/3af94751f085d24bc65d065ca6a938a8.

[25] Riccardo, V. et al. JET disruption studies in support of ITER. Plasma Physics and Controlled Fusion, **52** (2010)(12), 124018. http://stacks.iop.org/0741-3335/52/i=12/a=124018.

[26] Helander, P. and Ward, D.J. Positron creation and annihilation in tokamak plasmas with runaway electrons. Physical Review Letters, **90** (2003), 135004. http://link.aps.org/doi_notnow/10.1103/PhysRevLett.90.135004.

[27] Hastie, R.J. Sawtooth instability in tokamak plasmas. Astrophysics and space science, **256** (1998)(1-2), 177–204. http://dx.doi_notnow.org/10.1023/A:1001728227899.

[28] Nave, M. et al. Role of sawtooth in avoiding impurity accumulation and maintaining good confinement in JET radiative mantle discharges. Nuclear Fusion, **43** (2003)(10), 1204. http://stacks.iop.org/0029-5515/43/i=10/a=023.

[29] Sauter, O. et al. Control of neoclassical tearing modes by sawtooth control. Physical Review Letters, **88** (2002)(10), 105001. http://prl.aps.org/abstract/PRL/v88/i10/e105001.

[30] Gude, A. et al. Temporal evolution of neoclassical tearing modes and its effect on confinement reduction in ASDEX Upgrade. Nuclear Fusion, **42** (2002)(7), 833. http://stacks.iop.org/0029-5515/42/i=7/a=306.

[31] Chapman, I.T. Controlling sawtooth oscillations in tokamak plasmas. Plasma Physics and Controlled Fusion, **53** (2011)(1), 013001. http://stacks.iop.org/0741-3335/53/i=1/a=013001.

[32] von Goeler, S., Stodiek, W. and Sauthoff, N. Studies of internal disruptions and m=1 oscillations in tokamak discharges with Soft-X-Ray tecniques. Physical Review Letters, **33** (1974)(20), 1201–1203. http://prola.aps.org/abstract/PRL/v33/i20/p1201_1.

[33] Igochine, V. et al. Transition from quasiperiodicity to chaos just before sawtooth crash in the ASDEX Upgrade tokamak. Nuclear Fusion, **48** (2008)(6), 062001 (5pp). http://stacks.iop.org/0029-5515/48/062001.

[34] Igochine, V. et al. The role of stochastization in fast MHD phenomena on ASDEX Upgrade. In *Proceedings of the 23st IAEA Fusion Energy Conference*, EX/P9-10. Genf, Switzerland (2008) http://www-pub.iaea.org/MTCD/Meetings/FEC2008/ex_p9-10.pdf.

[35] Papp, G. et al. Analysis of sawtooth precursor activity in ASDEX Upgrade using bandpower correlation method. In *Europhysics Conference Abstracts*, volume 33E (2009) page P1.157. http://epsppd.epfl.ch:80/Sofia/pdf/P1_157.pdf.

[36] Sun, Y. et al. Observation of heat transfer across X point of the islands during sawtooth crash on the HT-7 tokamak. Plasma Physics and Controlled Fusion, **51** (2009)(6), 065001. http://stacks.iop.org/0741-3335/51/065001/.

[37] Buttery, R. et al. Onset of neoclassical tearing modes on JET. Nuclear Fusion, **43** (2003)(2), 69. http://stacks.iop.org/0029-5515/43/i=2/a=301.

[38] Chapman, I.T. et al. Magnetic reconnection triggering magnetohydrodynamic instabilities during a sawtooth crash in a tokamak plasma. Physical Review Letters, **105** (2010)(25), 255002. http://prl.aps.org/abstract/PRL/v105/i25/e255002.

[39] Kruskal, M.D. and Kulsrud, R.M. Equilibrium of a magnetically confined plasma in a toroid. Physics of Fluids, **1** (1958)(4), 265–274. http://link.aip.org/link/?PFL/1/265/1.

[40] Greene, J.M. and Johnson, J.L. Stability criterion for arbitrary hydromagnetic equilibria. Physics of Fluids, **5** (1962)(5), 510–517. http://link.aip.org/link/?PFL/5/510/1.

[41] Balescu, R., Vlad, M. and Spineanu, F. Tokamap: A Hamiltonian twist map for magnetic field lines in a toroidal geometry. Phys. Rev. E, **58** (1998)(1), 951–964. http://pre.aps.org/abstract/PRE/v58/i1/p951_1.

[42] Boozer, A.H. Evaluation of the structure of ergodic fields. Physics of Fluids, **26** (1983)(5), 1288–1291. http://link.aip.org/link/?PFL/26/1288/1.

[43] Kerst, D.W. The influence of errors on plasma-confining magnetic fields. Journal of Nuclear Energy. Part C, Plasma Physics, Accelerators, Thermonuclear Research, **4** (1962)(4), 253–262. http://stacks.iop.org/0368-3281/4/i=4/a=303.

[44] Elsasser, K. Magnetic field line flow as a Hamiltonian problem. Plasma Physics and Controlled Fusion, **28** (1986)(12A), 1743–1752. http://stacks.iop.org/0741-3335/28/i=12A/a=001.

[45] Martin, T.J. and Taylor, J.B. Ergodic behaviour in a magnetic limiter. Plasma Physics and Controlled Fusion, **26** (1984)(1B), 321. http://stacks.iop.org/0741-3335/26/i=1B/a=005.

[46] Abdullaev, S.S. and Zaslavsky, G.M. Application of the separatrix map to study perturbed magnetic field lines near the separatrix. Physics of Plasmas, **3** (1996)(2), 516–528. http://link.aip.org/link/?PHP/3/516/1.

[47] Abdullaev, S.S. et al. Twist mapping for the dynamics of magnetic field lines in a tokamak ergodic divertor. Physics of Plasmas, **5** (1998)(1), 196–210. http://link.aip.org/link/?PHP/5/196/1.

[48] Schuster, H.G. and Just, W. *Deterministic chaos*. Wiley-VCH, Germany, 4th edition (2004).

[49] Tél, T. and Gruiz, M. *Chaotic dynamics*. Cambridge University Press, Cambridge, paperback edition (2006). http://www.cambridge.org/gb/knowledge/isbn_notnow/item1151783/.

[50] Chirikov, B.V. Research concerning the theory of nonlinear resonance and stochasticity. Technical Report 267, Insitute of Nuclear Physics, Novosibirsk (1969). http://www.quantware.ups-tlse.fr/chirikov/refs/chi1969.pdf Engl. Transl., CERN Trans. 71 - 40, Geneva, October (1971) http://www.quantware.ups-tlse.fr/chirikov/refs/chi1969e.pdf.

[51] Chirikov, B.V. A universal instability of many-dimensional oscillator systems. Physics Reports, **52** (1979)(5), 263 – 379. http://www.sciencedirect.com/science/article/B6TVP-46SPHBD-5V/2/cf84bfb81360e901a1e2b66baa0d7ce6.

[52] Kolmogorov, A.N. General theory of dynamical systems in classical mechanics. In *Proceedings of the 1954 International Congress of Mathematics*, volume 1. North Holland, Amsterdam (1957) pages 315–333. http://ntrs.nasa.gov/archive/nasa/casi.ntrs.nasa.gov/19720025583_1972025583.pdf.

[53] Arnold, V.I. Small denominators II: Proof of a theorem by A.N. Kolmogorov on the preservation of conditionally-periodic motion under small perturbation of the Hamiltonian. Russ. Math. Surveys, **18** (1963)(9). [Uspekhi Mat. Nauk 18 13 (1963)] http://iopscience.iop.org/0036-0279/18/5/R02.

[54] Moser, J. On invariant curves of area preserving mappings of an annulus. Nachr. Akad. Wiss. Göttingen II Math. Phys., **1** (1962)(1), 1–20.

[55] Igochine, V. et al. Stochastic sawtooth reconnection in ASDEX Upgrade. Nuclear Fusion, **47** (2007)(1), 23–32. http://iopscience.iop.org/0029-5515/47/1/004.

[56] Dumbrajs, O. et al. Diffusion in a stochastic magnetic field in ASDEX Upgrade. Nuclear Fusion, **48** (2008)(2), 024011 (7pp). http://www.iop.org/EJ/abstract/0029-5515/48/2/024011.

[57] Igochine, V. et al. Stochastization as a possible cause for fast reconnection during MHD mode activity in the ASDEX Upgrade

tokamak. Nuclear Fusion, **46** (2006)(7), 741–751. http://www.iop.org/EJ/abstract/0029-5515/46/7/006.

[58] Finken, K. et al. *The structure of magnetic field in the TEXTOR-DED.* Grafische Medien, Forschungszentrum Jülich GmbH, Jülich (2005). http://www.fz-juelich.de/zb/datapool/page/439/00312_Finken.pdf.

[59] Moyer, R.A. et al. Edge localized mode control with an edge resonant magnetic perturbation. Physics of Plasmas, **12** (2005)(5), 056119. http://link.aip.org/link/?PHP/12/056119/1.

[60] Evans, T.E. et al. The physics of edge resonant magnetic perturbations in hot tokamak plasmas. Physics of Plasmas, **13** (2006)(5), 056121. http://link.aip.org/link/?PHP/13/056121/1.

[61] Schaffer, M. et al. Study of in-vessel nonaxisymmetric ELM suppression coil concepts for ITER. Nuclear Fusion, **48** (2008)(2), 024004. http://stacks.iop.org/0029-5515/48/i=2/a=024004.

[62] Fenstermacher, M.E. et al. Effect of island overlap on edge localized mode suppression by resonant magnetic perturbations in DIII-D. Physics of Plasmas, **15** (2008)(5), 056122. http://link.aip.org/link/?PHP/15/056122/1.

[63] Nardon, E. et al. Edge localized mode control experiments on MAST using resonant magnetic perturbations from in-vessel coils. Plasma Physics and Controlled Fusion, **51** (2009)(12), 124010. http://stacks.iop.org/0741-3335/51/i=12/a=124010.

[64] Wesson, J. et al. Disruptions in JET. Nuclear Fusion, **29** (1989)(4), 641. http://stacks.iop.org/0029-5515/29/i=4/a=009.

[65] de Vries, P. et al. Survey of disruption causes at JET. Nuclear Fusion, **51** (2011)(5), 053018. http://stacks.iop.org/0029-5515/51/i=5/a=053018.

[66] Lehnen, M. et al. Disruption heat loads and their mitigation in JET with the ITER-like wall. Journal of Nuclear Materials, (2013). (Corrected proof) http://www.sciencedirect.com/science/article/pii/S002231151300024X.

[67] Putvinski, S. et al. Halo current, runaway electrons and disruption mitigation in ITER. Plasma Physics and Controlled Fusion, **39** (1997)(12B), B157. http://stacks.iop.org/0741-3335/39/i=12B/a=013.

[68] Riccardo, V. et al. Progress in understanding halo current at JET. Nuclear Fusion, **49** (2009)(5), 055012. http://stacks.iop.org/0029-5515/49/i=5/a=055012.

[69] Forster, M. et al. Energy deposition and radial decay of runaway electrons in a disruption at textor. Nuclear Fusion, **51** (2011)(4), 043003. http://stacks.iop.org/0029-5515/51/i=4/a=043003.

[70] Bazylev, B. et al. Modeling of the impact of runaway electrons on the ILW in JET. Journal of Nuclear Materials, (2013). (Corrected proof) http://www.sciencedirect.com/science/article/pii/S0022311513000433.

[71] Bakhtiari, M. et al. Role of Bremsstrahlung radiation in limiting the energy of runaway electrons in tokamaks. Physical Review Letters, **94** (2005)(21), 215003. http://prl.aps.org/abstract/PRL/v94/i21/e215003.

[72] Dreicer, H. Electron and ion runaway in a fully ionized gas. II. Phys. Rev., **117** (1960)(2), 329–342. http://prola.aps.org/abstract/PR/v117/i2/p329_1.

[73] Connor, J. and Hastie, R. Relativistic limitations on runaway electrons. Nuclear Fusion, **15** (1975)(3), 415. http://stacks.iop.org/0029-5515/15/i=3/a=007.

[74] Harvey, R.W. et al. Runaway electron production in DIII-D killer pellet experiments, calculated with the CQL3D/KPRAD model. Physics of Plasmas, **7** (2000)(11), 4590–4599. http://link.aip.org/link/?PHP/7/4590/1.

[75] Smith, H. Runaway electrons and Alfvén eigenmodes in tokamaks. Ph.D. thesis, Chalmers University of Technology, Göteborg, Sweden (2006). http://publications.lib.chalmers.se/cpl/record/index.xsql?pubid=23189.

[76] Smith, H. et al. Runaway electron generation in a cooling plasma. Physics of Plasmas, **12** (2005)(12), 122505. http://link.aip.org/link/?PHP/12/122505/1.

[77] Smith, H.M. and Verwichte, E. Hot tail runaway electron generation in tokamak disruptions. Physics of Plasmas, **15** (2008)(7), 072502. http://link.aip.org/link/?PHP/15/072502/1.

[78] Gryaznykh, D.A. Cross section for the production of electron-positron pairs by electrons in the field of a nucleus. Physics of Atomic Nuclei, **61** (1998)(3), 394–399. [Yad. Fiz. 61, 454 (1998)].

[79] Fülöp, T. et al. Destabilization of magnetosonic-whistler waves by a relativistic runaway beam. Physics of Plasmas, **13** (2006)(6), 062506. http://link.aip.org/link/?PHP/13/062506/1.

[80] Jaspers, R. et al. A synchrotron radiation diagnostic to observe relativistic runaway electrons in a tokamak plasma. Review of Scientific Instruments, **72** (2001)(1), 466–470. http://link.aip.org/link/?RSI/72/466/1.

[81] Pankratov, I.M. Analysis of the synchrotron radiation spectra of runaway electrons. Plasma Physics Reports, **25** (1999)(2), 145–148. [Translated from Fizika Plazmy, Vol. 25, No 2, 1999, pp. 165–168.].

[82] Helander, P., Eriksson, L.G. and Andersson, F. Suppression of runaway electron avalanches by radial diffusion. Physics of Plasmas, **7** (2000)(10), 4106–4111. http://link.aip.org/link/?PHP/7/4106/1.

[83] Fehér, T. et al. Simulation of runaway electron generation during plasma shutdown by impurity injection in ITER. Plasma Physics and Controlled Fusion, **53** (2011)(3), 035014. http://stacks.iop.org/0741-3335/53/i=3/a=035014.

[84] Rechester, A.B. and Rosenbluth, M.N. Electron heat transport in a tokamak with destroyed magnetic surfaces. Physical Review Letters, **40** (1978)(1), 38–41. http://prl.aps.org/abstract/PRL/v40/i1/p38_1.

[85] Eriksson, L.G. and Helander, P. Simulation of runaway electrons during tokamak disruptions. Computer Physics Communications, **154** (2003)(3), 175–196. http://www.sciencedirect.com/science/article/B6TJ5-494HRX8-1/2/cdfd3f57818537f8be913c8d0a9c6f3d.

[86] Eriksson, L.G. et al. Current dynamics during disruptions in large tokamaks. Physical Review Letters, **92** (2004)(20), 205004. `http://prl.aps.org/abstract/PRL/v92/i20/e205004`.

[87] Decker, J. and Peysson, Y. LUKE: a fast numerical solver for the 3-D relativistic bounce-averaged electron drift kinetic equation. Technical Report EUR-CEA-FC-1736, EURATOM-CEA (2004).

[88] Peysson, Y., Decker, J. and Harvey, R.W. Advanced 3-d electron fokker-planck transport calculations. AIP Conference Proceedings, **694** (2003)(1), 495–498. `http://link.aip.org/link/?APC/694/495/1`.

[89] Peysson, Y. and Decker, J. Calculation of rf current drive in tokamaks. AIP Conference Proceedings, **1069** (2008)(1), 176–187. `http://link.aip.org/link/?APC/1069/176/1`.

[90] Smith, H.M. et al. Runaway electron generation in tokamak disruptions. Plasma Physics and Controlled Fusion, **51** (2009)(12), 124008. `http://stacks.iop.org/0741-3335/51/i=12/a=124008`.

[91] Andersson, F., Helander, P. and Eriksson, L.G. Damping of relativistic electron beams by synchrotron radiation. Physics of Plasmas, **8** (2001)(12), 5221–5229. `http://link.aip.org/link/?PHP/8/5221/1`.

[92] Pauli, W. *Theory of relativity*. Dover Publications, Inc., New York (1981).

[93] Bakhtiari, M., Kramer, G.J. and Whyte, D.G. Momentum-space study of the effect of bremsstrahlung radiation on the energy of runaway electrons in tokamaks. Physics of Plasmas, **12** (2005)(10), 102503. `http://link.aip.org/link/?PHP/12/102503/1`.

[94] Drevlak, M. Thermal load on the W7-X vessel from NBI losses. In *Europhysics Conference Abstracts*, volume 33E (2009) pages P–4.211. `http://epsppd.epfl.ch/Sofia/pdf/P4_211.pdf`.

[95] Drevlak, M. Optimization of heterogenous magnet systems. In *Proceedings of the 12th International Stellarator Workshop*, P1-17. Madison, Wisconsin (1999) `http://www-fusion.ciemat.es/SW2005/conferences/madison99/Papers/Drevlak.pdf`.

[96] Drevlak, M., Monticello, D. and Reiman, A. PIES free boundary stellarator equilibria with improved initial conditions. Nuclear Fusion, **45** (2005)(7), 731–740. http://stacks.iop.org/0029-5515/45/731.

[97] Dewar, R.L. and Hudson, S.R. Stellarator symmetry. Physica D: Nonlinear Phenomena, **112** (1998)(1-2), 275 – 280. http://www.sciencedirect.com/science/article/B6TVK-3SYS86V-1G/2/7a73fe5163a168731e64c7909f7264b4.

[98] Forster, M. et al. Runaway electron transport in turbulent and resonantly perturbed magnetic topologies of TEXTOR. Nuclear Fusion, **52** (2012)(8), 083016. http://stacks.iop.org/0029-5515/52/i=8/a=083016.

[99] Abdullaev, S.S. and Finken, K.H. Hamiltonian guiding center equations in a toroidal system. Physics of Plasmas, **9** (2002)(10), 4193–4204. http://link.aip.org/link/?PHP/9/4193/1.

[100] Abdullaev, S.S., Wingen, A. and Spatschek, K.H. Mapping of drift surfaces in toroidal systems with chaotic magnetic fields. Physics of Plasmas, **13** (2006)(4), 042509. http://link.aip.org/link/?PHP/13/042509/1.

[101] Wingen, A. et al. Influence of stochastic magnetic fields on relativistic electrons. Nuclear Fusion, **46** (2006)(11), 941. http://stacks.iop.org/0029-5515/46/i=11/a=008.

[102] Hirshman, S.P., van RIJ, W.I. and Merkel, P. Three-dimensional free boundary calculations using a spectral Green's function method. Computer Physics Communications, **43** (1986)(1), 143 – 155. http://www.sciencedirect.com/science/article/B6TJ5-46G02MT-4D/2/22b74c1dbc14330349d57c300055db68.

[103] Laurent, L. and Rax, J.M. Stochastic instability of runaway electrons in tokamaks. EPL (Europhysics Letters), **11** (1990)(3), 219. http://stacks.iop.org/0295-5075/11/i=3/a=006.

[104] Kurzan, B., Steuer, K.H. and Fussmann, G. Dynamics of runaway electrons in the magnetic field of a tokamak. Phys. Rev. Lett., **75** (1995), 4626–4629. http://link.aps.org/doi/10.1103/PhysRevLett.75.4626.

[105] Martin-Solis, J.R. et al. Energy limits on runaway electrons in tokamak plasmas. Physics of Plasmas, **6** (1999)(1), 238–252. http://link.aip.org/link/?PHP/6/238/1.

[106] Martin-Solis, J.R. and Sanchez, R. Pitch angle scattering and synchrotron radiation of relativistic runaway electrons in tokamak stochastic magnetic fields. Physics of Plasmas, **15** (2008)(11), 112505. http://link.aip.org/link/?PHP/15/112505/1.

[107] Abdullaev, S. et al. Overview of magnetic structure induced by the TEXTOR-DED and the related transport. Nuclear Fusion, **43** (2003)(5), 299–313. http://stacks.iop.org/0029-5515/43/299.

[108] Chu, M. et al. Response of a resistive and rotating tokamak to external magnetic perturbations below the Alfvén frequency. Nuclear Fusion, **51** (2011)(7), 073036. http://stacks.iop.org/0029-5515/51/i=7/a=073036.

[109] Heyn, M. et al. On the confinement of passing alpha particles in a tokamak-reactor with resonant magnetic field perturbations shielded by plasma currents. Nuclear Fusion, **52** (2012)(5), 054010. http://stacks.iop.org/0029-5515/52/i=5/a=054010.

[110] Liu, Y.Q. et al. Toroidal modeling of plasma response and resonant magnetic perturbation field penetration. Plasma Physics and Controlled Fusion, **54** (2012)(12), 124013. http://stacks.iop.org/0741-3335/54/i=12/a=124013.

[111] de Rover, M., Cardozo, N.J.L. and Montvai, A. Motion of relativistic particles in axially symmetric and perturbed magnetic fields in a tokamak. Physics of Plasmas, **3** (1996)(12), 4478–4488. http://link.aip.org/link/?PHP/3/4478/1.

[112] Guan, X., Qin, H. and Fisch, N.J. Phase-space dynamics of runaway electrons in tokamaks. Physics of Plasmas, **17** (2010)(9), 092502. http://link.aip.org/link/?PHP/17/092502/1.

[113] Knoepfel, H. and Spong, D. Runaway electrons in toroidal discharges. Nuclear Fusion, **19** (1979)(6), 785. http://stacks.iop.org/0029-5515/19/i=6/a=008.

[114] Izzo, V. et al. Runaway electron confinement modelling for rapid shutdown scenarios in DIII-D, Alcator C-Mod and ITER. Nuclear Fusion, **51** (2011)(6), 063032. http://stacks.iop.org/0029-5515/51/i=6/a=063032.

[115] Zhou, R.J. et al. Investigation of ring-like runaway electron beams in the EAST tokamak. Plasma Physics and Controlled Fusion, **55** (2013)(5), 055006. http://stacks.iop.org/0741-3335/55/i=5/a=055006.

[116] Li, E., Zhou, R. and Hu, L. Evidence for a resonant cyclotron interaction between runaway electrons and MHD modes in the Experimental Advanced Superconducting Tokamak. Physics of Plasmas, **18** (2011)(9), 092501. http://link.aip.org/link/?PHP/18/092501/1.

[117] Zhou, R.J. et al. Effect of magnetic fluctuations on the confinement and dynamics of runaway electrons in the HT-7 tokamak. Physics of Plasmas, **20** (2013)(3), 032511. http://link.aip.org/link/?PHP/20/032511/1.

[118] Koslowski, R., Zeng, L. and TEXTOR Team. Characterisation of dynamics of runaway beam plasma (2012.09.11.). EFDA project meeting A7/1, JET-EFDA Culham Science Centre, OX15 3DB, Abingdon, UK.

[119] Kiptily, V. et al. Runaway measurements on JET (2012.05.14–17.). 22nd ITPA Diagnostic meeting, Moscow, Russia.

[120] Polevoi, A. Technical Report 22KZK3, ITER Documentation System (IDM) (2002).

[121] Polevoi, A. et al. ITER confinement and stability modelling. J. Plasma Fusion Res. Series, **5** (2002), 82–87. http://www.jspf.or.jp/JPFRS/PDF/Vol5/jpfrs2002_05-082.pdf.

[122] Misguich, J.H. et al. Noble cantor sets acting as partial internal transport barriers in fusion plasmas. Plasma Physics and Controlled Fusion, **44** (2002)(7), L29. http://stacks.iop.org/0741-3335/44/i=7/a=101.

[123] Kurki-Suonio, T. et al. ASCOT simulations of fast ion power loads to the plasma-facing components in ITER. Nuclear Fusion,

49 (2009)(9), 095001. http://stacks.iop.org/0029-5515/49/i=9/a=095001.

[124] Shinohara, K. et al. Effects of complex symmetry-breakings on alpha particle power loads on first wall structures and equilibrium in iter. Nuclear Fusion, **51** (2011)(6), 063028. http://stacks.iop.org/0029-5515/51/i=6/a=063028.

[125] Tani, K. et al. Effects of ELM mitigation coils on energetic particle confinement in ITER steady-state operation. Nuclear Fusion, **52** (2012)(1), 013012. http://stacks.iop.org/0029-5515/52/i=1/a=013012.

[126] Asunta, O. et al. Simulations of fast ion wall loads in ASDEX Upgrade in the presence of magnetic perturbations due to ELM-mitigation coils. Nuclear Fusion, **52** (2012)(9), 094014. http://stacks.iop.org/0029-5515/52/i=9/a=094014.

[127] Koskela, T. et al. ITER edge-localized modes control coils: the effect on fast ion losses and edge confinement properties. Plasma Physics and Controlled Fusion, **54** (2012)(10), 105008. http://stacks.iop.org/0741-3335/54/i=10/a=105008.

[128] Snicker, A., Sipilä, S. and Kurki-Suonio, T. Orbit-following fusion alpha wall load simulation for iter scenario 4 including full orbit effects. Nuclear Fusion, **52** (2012)(9), 094011. http://stacks.iop.org/0029-5515/52/i=9/a=094011.

[129] Smith, H. et al. Runaway electrons and the evolution of the plasma current in tokamak disruptions. Physics of Plasmas, **13** (2006)(10), 102502. http://link.aip.org/link/?PHP/13/102502/1.

[130] Gál, K. et al. Runaway electron generation during plasma shutdown by killer pellet injection. Plasma Physics and Controlled Fusion, **50** (2008)(5), 055006. http://stacks.iop.org/0741-3335/50/i=5/a=055006.

[131] Helander, P. et al. Electron kinetics in a cooling plasma. Physics of Plasmas, **11** (2004)(12), 5704–5709. http://link.aip.org/link/?PHP/11/5704/1.

[132] Huba, J.D. *NRL Plasma Formulary*. NRL/PU/6790–00-426. Naval Research Laboratory, Washington DC, revised edition (2006). http://wwwppd.nrl.navy.mil/nrlformulary/.

[133] Summers, H.P. *The ADAS User Manual, version 2.6* (2004).
http://www.adas.ac.uk/manual.php.

[134] Gill, R. Generation and loss of runaway electrons following disruptions in JET. Nuclear Fusion, **33** (1993)(11), 1613. http://stacks.iop.org/0029-5515/33/i=11/a=I03.

[135] Gill, R. et al. Behaviour of disruption generated runaways in jet. Nuclear Fusion, **42** (2002)(8), 1039. http://stacks.iop.org/0029-5515/42/i=8/a=312.

[136] Riccardo, V. and contributors, J.E. Disruptions and disruption mitigation. Plasma Physics and Controlled Fusion, **45** (2003)(12A), A269. http://stacks.iop.org/0741-3335/45/i=12A/a=018.

[137] Plyusnin, V. et al. Study of runaway electron generation during major disruptions in JET. Nuclear Fusion, **46** (2006)(2), 277. http://stacks.iop.org/0029-5515/46/i=2/a=011.

[138] Lehnen, M. et al. Disruption mitigation by massive gas injection in jet. Nuclear Fusion, **51** (2011)(12), 123010. http://stacks.iop.org/0029-5515/51/i=12/a=123010.

[139] Matthews, G.F. et al. JET ITER-like wall–overview and experimental programme. Physica Scripta, **2011** (2011)(T145), 014001. http://stacks.iop.org/1402-4896/2011/i=T145/a=014001.

[140] de Vries, P.C. et al. The impact of the ITER-like wall at JET on disruptions. Plasma Physics and Controlled Fusion, **54** (2012)(12), 124032. http://stacks.iop.org/0741-3335/54/i=12/a=124032.

[141] Hollmann, E. et al. Measurements of injected impurity assimilation during massive gas injection experiments in DIII-D. Nuclear Fusion, **48** (2008)(11), 115007. http://stacks.iop.org/0029-5515/48/i=11/a=115007.

[142] Hutchinson, I.H. *Principles of Plasma Diagnostics*. Cambridge University Press, second edition (2002).

[143] Sokoll, M. MHD-Instabilitaten in magnetisch eingeschlossen Plasmen und ihre tomographische Rekonstruktion im Röntgenlicht.

Technical Report 1/309, Max Planck Insitut für Plasmaphysik, (IPP), Garching bei München (1997). http://edoc.mpg.de/display.epl?mode=doc&id=438832.

[144] Muck, A. et al. Sawtooth control experiments on ASDEX Upgrade. Plasma Physics and Controlled Fusion, **47** (2005)(10), 1633. http://stacks.iop.org/0741-3335/47/i=10/a=004.

[145] Eriksson, L.G. et al. On ion cyclotron current drive for sawtooth control. Nuclear Fusion, **46** (2006)(10), S951. http://stacks.iop.org/0029-5515/46/i=10/a=S12.

[146] Graves, J.P. et al. Sawtooth-control mechanism using toroidally propagating ion-cyclotron-resonance waves in tokamaks. Physical Review Letters, **102** (2009)(6), 065005. http://prl.aps.org/abstract/PRL/v102/i6/e065005.

[147] Chapman, I. et al. Sawtooth control and the interaction of energetic particles. Nuclear Fusion, **49** (2009)(3), 035006. http://stacks.iop.org/0029-5515/49/i=3/a=035006.

[148] Graves, J. et al. Experimental verification of sawtooth control by energetic particles in ion cyclotron resonance heated JET tokamak plasmas. Nuclear Fusion, **50** (2010)(5), 052002. http://stacks.iop.org/0029-5515/50/i=5/a=052002.

[149] Igochine, V. et al. Destabilization of fast particle stabilized sawteeth in ASDEX Upgrade with electron cyclotron current drive. Plasma Physics and Controlled Fusion, **53** (2011)(2), 022002. http://stacks.iop.org/0741-3335/53/i=2/a=022002.

[150] Chapman, I.T. et al. The physics of sawtooth stabilization. Plasma Physics and Controlled Fusion, **49** (2007)(12B), B385. http://stacks.iop.org/0741-3335/49/i=12B/a=S35.

[151] Kadomtsev, B.B. On disruptive instability in tokamaks. Soviet Journal of Plasma Physics, **1** (1975), 710–715. http://adsabs.harvard.edu/abs/1975SvJPP...1Q.710K.

[152] Xu, X. et al. Experimental investigation of m / n = 1/1 and high-order harmonic modes during the sawtooth oscillation in a low beta tokamak plasma. Plasma Physics and Controlled Fusion, **52** (2010)(1), 015008. http://stacks.iop.org/0741-3335/52/i=1/a=015008.

[153] Lichtenberg, A. Stochasticity as the mechanism for the disruptive phase of the m = 1 tokamak oscillations. Nuclear Fusion, **24** (1984)(10), 1277. http://stacks.iop.org/0029-5515/24/i=10/a=004.

[154] Lichtenberg, A. et al. The role of stochasticity in sawtooth oscillations. Nuclear Fusion, **32** (1992)(3), 495. http://stacks.iop.org/0029-5515/32/i=3/a=I12.

[155] Igochine, V. et al. Hotlink based soft X-ray diagnostic on AS-DEX Upgrade. Technical Report 1/338, Max Planck Insitut für Plasmaphysik, (IPP), Garching bei München (2010). http://edoc.mpg.de/display.epl?mode=doc&id=476537.

[156] Mallat, S. *A wavelet tour of signal processing*. Academic Press, second edition (2001).

[157] Varela, P. Automatic time-frequency analysis for plasma density profile evaluation from microwave reflectometry. Ph.D. thesis, Universidade Técnica de Lisboa (2002).

[158] Dijkstra, E.W. A note on two problems in connexion with graphs. Numerische Mathematik, **1** (1959), 269–271. http://www-m3.ma.tum.de/foswiki/pub/MN0506/WebHome/dijkstra.pdf.

[159] Pokol, G. et al. Application of a bandpower correlation method to the statistical analysis of MHD bursts in quiescent Wendelstein-7 AS stellarator plasmas. Plasma Physics and Controlled Fusion, **49** (2007)(9), 1391–1408. http://www.iop.org/EJ/abstract/0741-3335/49/9/003/.

[160] Hastie, R.J. et al. Stability of ideal and resistive internal kink modes in toroidal geometry. Physics of Fluids, **30** (1987)(6), 1756–1766. http://link.aip.org/link/?PFL/30/1756/1.

[161] Kim, Y.C. and Powers, E.J. Digital bispectral analysis and its applications to nonlinear wave interactions. Plasma Science, IEEE Transactions on, **7** (1979)(2), 120–131. http://dx.doi_notnow.org/10.1109/TPS.1979.4317207.

[162] Pokol, G. et al. Experimental study and simulation of W7-AS transient MHD modes. AIP Conference Proceedings, **993** (2008)(1), 215–218. http://link.aip.org/link/?APC/993/215/1.

[163] Pokol, G. et al. A wavelet based method for detecting transient plasma waves and determining their spatial structure. In *Europhysics Conference Abstracts*, volume 34A. Dublin, Ireland (2010) page P5.129. http://ocs.ciemat.es/EPS2010PAP/pdf/P5.129.pdf.

[164] Schittenhelm, M. and Zohm, H. Analysis of coupled MHD modes with Mirnov probes in ASDEX Upgrade. Nuclear Fusion, **37** (1997)(9), 1255. http://stacks.iop.org/0029-5515/37/i=9/a=I06.

[165] Papp, G. et al. Low frequency sawtooth precursor in ASDEX Upgrade. In *5th IAEA Technical Meeting on Theory of Plasma Instabilities, IAEA-TM-40758*. Austin, USA (2011) page B4.1. http://http://w3fusion.ph.utexas.edu/ifs/iaeapi/papers/b4-1-papp-gergely-pi-paper.pdf.

[166] Park, H.K. et al. Self-organized T_e redistribution during driven reconnection processes in high-temperature plasmas. Physics of Plasmas, **13** (2006)(5), 055907. http://link.aip.org/link/?PHP/13/055907/1.

[167] Igochine, V. et al. Structure and dynamics of sawteeth crashes in ASDEX Upgrade. Physics of Plasmas, **17** (2010)(12), 122506. http://link.aip.org/link/?PHP/17/122506/1.

[168] Letsch, A. et al. Incomplete reconnection in sawtooth crashes in ASDEX Upgrade. Nuclear Fusion, **42** (2002)(9), 1055. http://stacks.iop.org/0029-5515/42/i=9/a=302.

[169] Gimblett, C.G. and Hastie, R.J. Calculation of the post-crash state and 1 1/2 D simulation of sawtooth cycles. Plasma Physics and Controlled Fusion, **36** (1994)(9), 1439. http://stacks.iop.org/0741-3335/36/i=9/a=005.

Included papers A–F

Paper A

Paper B

Paper C

Paper D

G. Papp, T. Fülöp, T. Fehér, P. C. de Vries, V. Riccardo, C. Reux, M. Lehnen, V. Kiptily, V. V. Pluysnin, B. Alper and JET EFDA contributors. The effect of ITER-like wall on runaway electron generation in JET. *Nuclear Fusion*, **submitted**, 2013.

Paper E

Paper F